System size and energy dependence of near-side dihadron correlations

(STAR Collaboration) Agakishiev, G.; ...; Planinić, Mirko; ...; Poljak, Nikola; ...; Zoulkarneeva, Y.

Journal article, Published version
Rad u časopisu, Objavljena verzija rada (izdavačev PDF)

Permanent link / Trajna poveznica: https://urn.nsk.hr/urn:nbn:hr:217:724657

Download date / Datum preuzimanja: **2025-04-01**

Repository / Repozitorij:

Repository of the Faculty of Science - University of Zagreb

System size and energy dependence of near-side dihadron correlations

G. Agakishiev,[17] M. M. Aggarwal,[29] Z. Ahammed,[47] A. V. Alakhverdyants,[17] I. Alekseev,[15] J. Alford,[18] B. D. Anderson,[18]
C. D. Anson,[27] D. Arkhipkin,[2] G. S. Averichev,[17] J. Balewski,[22] L. S. Barnby,[54] D. R. Beavis,[2] R. Bellwied,[43]
M. J. Betancourt,[22] R. R. Betts,[7] A. Bhasin,[16] A. K. Bhati,[29] H. Bichsel,[49] J. Bielcik,[9] J. Bielcikova,[10] L. C. Bland,[2]
M. Bombara,[54] I. G. Bordyuzhin,[15] W. Borowski,[40] J. Bouchet,[18] E. Braidot,[26] A. V. Brandin,[25] S. G. Brovko,[4] E. Bruna,[52]
S. Bueltmann,[28] I. Bunzarov,[17] T. P. Burton,[2] X. Z. Cai,[39] H. Caines,[52] M. Calderón de la Barca Sánchez,[4] D. Cebra,[4]
R. Cendejas,[5] M. C. Cervantes,[41] P. Chaloupka,[10] S. Chattopadhyay,[47] H. F. Chen,[37] J. H. Chen,[39] J. Y. Chen,[51] L. Chen,[51]
J. Cheng,[44] M. Cherney,[8] A. Chikanian,[52] W. Christie,[2] P. Chung,[10] M. J. M. Codrington,[41] R. Corliss,[22] J. G. Cramer,[49]
H. J. Crawford,[3] X. Cui,[37] A. Davila Leyva,[42] L. C. De Silva,[43] R. R. Debbe,[2] T. G. Dedovich,[17] J. Deng,[38]
A. A. Derevschikov,[31] R. Derradi de Souza,[6] S. Dhamija,[14] L. Didenko,[2] P. Djawotho,[41] X. Dong,[21] J. L. Drachenberg,[41]
J. E. Draper,[4] C. M. Du,[20] L. E. Dunkelberger,[5] J. C. Dunlop,[2] L. G. Efimov,[17] M. Elnimr,[50] J. Engelage,[3] G. Eppley,[35]
L. Eun,[21] O. Evdokimov,[7] R. Fatemi,[19] J. Fedorisin,[17] R. G. Fersch,[19] P. Filip,[17] E. Finch,[52] Y. Fisyak,[2] C. A. Gagliardi,[41]
L. Gaillard,[54] D. R. Gangadharan,[27] F. Geurts,[35] P. Ghosh,[47] S. Gliske,[1] Y. N. Gorbunov,[8] O. G. Grebenyuk,[21] D. Grosnick,[46]
A. Gupta,[16] S. Gupta,[16] W. Guryn,[2] B. Haag,[4] O. Hajkova,[9] A. Hamed,[41] L.-X. Han,[39] J. W. Harris,[52] J. P. Hays-Wehle,[22]
S. Heppelmann,[30] A. Hirsch,[32] G. W. Hoffmann,[42] D. J. Hofman,[7] S. Horvat,[52] B. Huang,[37] H. Z. Huang,[5] T. J. Humanic,[27]
L. Huo,[41] G. Igo,[5] W. W. Jacobs,[14] C. Jena,[12] P. G. Jones,[54] J. Joseph,[18] E. G. Judd,[3] S. Kabana,[40] K. Kang,[44] J. Kapitan,[10]
K. Kauder,[7] H. W. Ke,[51] D. Keane,[18] A. Kechechyan,[17] D. Kettler,[49] D. P. Kikola,[32] J. Kiryluk,[21] A. Kisiel,[48] V. Kizka,[17]
S. R. Klein,[21] D. D. Koetke,[46] T. Kollegger,[11] J. Konzer,[32] I. Koralt,[28] L. Koroleva,[15] W. Korsch,[19] L. Kotchenda,[25]
P. Kravtsov,[25] K. Krueger,[1] L. Kumar,[18] M. A. C. Lamont,[2] J. M. Landgraf,[2] S. LaPointe,[50] J. Lauret,[2] A. Lebedev,[2]
R. Lednicky,[17] J. H. Lee,[2] W. Leight,[22] M. J. LeVine,[2] C. Li,[37] L. Li,[42] W. Li,[39] X. Li,[32] X. Li,[38] Y. Li,[44] Z. M. Li,[51]
L. M. Lima,[36] M. A. Lisa,[27] F. Liu,[51] T. Ljubicic,[2] W. J. Llope,[35] R. S. Longacre,[2] Y. Lu,[37] E. V. Lukashov,[25] X. Luo,[37]
G. L. Ma,[39] Y. G. Ma,[39] D. P. Mahapatra,[12] R. Majka,[52] O. I. Mall,[4] S. Margetis,[18] C. Markert,[42] H. Masui,[21] H. S. Matis,[21]
D. McDonald,[35] T. S. McShane,[8] N. G. Minaev,[31] S. Mioduszewski,[41] M. K. Mitrovski,[2] Y. Mohammed,[41] B. Mohanty,[47]
M. M. Mondal,[47] B. Morozov,[15] D. A. Morozov,[31] M. G. Munhoz,[36] M. K. Mustafa,[32] M. Naglis,[21] B. K. Nandi,[13]
C. Nattrass,[52] Md. Nasim,[47] T. K. Nayak,[47] L. V. Nogach,[31] S. B. Nurushev,[31] G. Odyniec,[21] A. Ogawa,[2] K. Oh,[33] A. Ohlson,[52]
V. Okorokov,[25] E. W. Oldag,[42] R. A. N. Oliveira,[36] D. Olson,[21] M. Pachr,[9] B. S. Page,[14] S. K. Pal,[47] Pan,[5] Y. Pandit,[18]
Y. Panebratsev,[17] T. Pawlak,[48] H. Pei,[7] C. Perkins,[3] W. Peryt,[48] P. Pile,[2] M. Planinic,[53] J. Pluta,[48] D. Plyku,[28] N. Poljak,[53]
J. Porter,[21] A. M. Poskanzer,[21] C. B. Powell,[21] D. Prindle,[49] C. Pruneau,[50] N. K. Pruthi,[29] P. R. Pujahari,[13] J. Putschke,[50]
H. Qiu,[20] R. Raniwala,[34] S. Raniwala,[34] R. L. Ray,[42] R. Redwine,[22] R. Reed,[4] C. K. Riley,[52] H. G. Ritter,[21] J. B. Roberts,[35]
O. V. Rogachevskiy,[17] J. L. Romero,[4] L. Ruan,[2] J. Rusnak,[10] N. R. Sahoo,[47] I. Sakrejda,[21] S. Salur,[21] J. Sandweiss,[52]
E. Sangaline,[4] A. Sarkar,[13] J. Schambach,[42] R. P. Scharenberg,[32] A. M. Schmah,[21] N. Schmitz,[23] T. R. Schuster,[11] J. Seele,[22]
J. Seger,[8] P. Seyboth,[23] N. Shah,[5] E. Shahaliev,[17] M. Shao,[37] B. Sharma,[29] M. Sharma,[50] S. S. Shi,[51] Q. Y. Shou,[39]
E. P. Sichtermann,[21] R. N. Singaraju,[47] M. J. Skoby,[32] N. Smirnov,[52] D. Solanki,[34] P. Sorensen,[2] U. G. deSouza,[36]
H. M. Spinka,[1] B. Srivastava,[32] T. D. S. Stanislaus,[46] S. G. Steadman,[22] J. R. Stevens,[14] R. Stock,[11] M. Strikhanov,[25]
B. Stringfellow,[32] A. A. P. Suaide,[36] M. C. Suarez,[7] M. Sumbera,[10] X. M. Sun,[21] Y. Sun,[37] Z. Sun,[20] B. Surrow,[22]
D. N. Svirida,[15] T. J. M. Symons,[21] A. Szanto de Toledo,[36] J. Takahashi,[6] A. H. Tang,[2] Z. Tang,[37] L. H. Tarini,[50]
T. Tarnowsky,[24] D. Thein,[42] J. H. Thomas,[21] J. Tian,[39] A. R. Timmins,[43] D. Tlusty,[10] M. Tokarev,[17] S. Trentalange,[5]
R. E. Tribble,[41] P. Tribedy,[47] B. A. Trzeciak,[48] O. D. Tsai,[5] T. Ullrich,[2] D. G. Underwood,[1] G. Van Buren,[2] G. van
Nieuwenhuizen,[22] J. A. Vanfossen Jr.,[18] R. Varma,[13] G. M. S. Vasconcelos,[6] A. N. Vasiliev,[31] F. Videbæk,[2] Y. P. Viyogi,[47]
S. Vokal,[17] S. A. Voloshin,[50] A. Vossen,[14] M. Wada,[42] G. Wang,[5] H. Wang,[24] J. S. Wang,[20] Q. Wang,[32] X. L. Wang,[37]
Y. Wang,[44] G. Webb,[19] J. C. Webb,[2] G. D. Westfall,[24] C. Whitten Jr.,[5] H. Wieman,[21] S. W. Wissink,[14] R. Witt,[45] W. Witzke,[19]
Y. F. Wu,[51] Z. Xiao,[44] W. Xie,[32] H. Xu,[20] N. Xu,[21] Q. H. Xu,[38] W. Xu,[5] Y. Xu,[37] Z. Xu,[2] L. Xue,[39] Y. Yang,[20] Y. Yang,[51]
P. Yepes,[35] Y. Yi,[32] K. Yip,[2] I.-K. Yoo,[33] M. Zawisza,[48] H. Zbroszczyk,[48] W. Zhan,[20] J. B. Zhang,[51] S. Zhang,[39] W. M. Zhang,[18]
X. P. Zhang,[44] Y. Zhang,[37] Z. P. Zhang,[37] F. Zhao,[5] J. Zhao,[39] C. Zhong,[39] X. Zhu,[44] Y. H. Zhu,[39] and Y. Zoulkarneeva[17]

(STAR Collaboration)

[1]*Argonne National Laboratory, Argonne, Illinois 60439, USA*
[2]*Brookhaven National Laboratory, Upton, New York 11973, USA*
[3]*University of California, Berkeley, California 94720, USA*
[4]*University of California, Davis, California 95616, USA*
[5]*University of California, Los Angeles, California 90095, USA*
[6]*Universidade Estadual de Campinas, CEP 13083-970 Sao Paulo, Brazil*
[7]*University of Illinois at Chicago, Chicago, Illinois 60607, USA*
[8]*Creighton University, Omaha, Nebraska 68178, USA*
[9]*Czech Technical University in Prague, FNSPE, Prague, CZ-115 19, Czech Republic*
[10]*Nuclear Physics Institute AS CR, CZ-250 68 Řež/Prague, Czech Republic*
[11]*University of Frankfurt, D-60325 Frankfurt, Germany*
[12]*Institute of Physics, Bhubaneswar 751005, India*

[13]*Indian Institute of Technology, Mumbai 400076, India*

[14]*Indiana University, Bloomington, Indiana 47408, USA*

[15]*Alikhanov Institute for Theoretical and Experimental Physics, Moscow 117218, Russia*

[16]*University of Jammu, Jammu 180001, India*

[17]*Joint Institute for Nuclear Research, Dubna 141 980, Russia*

[18]*Kent State University, Kent, Ohio 44242, USA*

[19]*University of Kentucky, Lexington, Kentucky 40506-0055, USA*

[20]*Institute of Modern Physics, Lanzhou 730000, China*

[21]*Lawrence Berkeley National Laboratory, Berkeley, California 94720, USA*

[22]*Massachusetts Institute of Technology, Cambridge, Massachusetts 02139-4307, USA*

[23]*Max-Planck-Institut für Physik, D-80805 Munich, Germany*

[24]*Michigan State University, East Lansing, Michigan 48824, USA*

[25]*Moscow Engineering Physics Institute, Moscow 115409, Russia*

[26]*NIKHEF and Utrecht University, 1098 XG Amsterdam, The Netherlands*

[27]*Ohio State University, Columbus, Ohio 43210, USA*

[28]*Old Dominion University, Norfolk, Virginia, 23529, USA*

[29]*Panjab University, Chandigarh 160014, India*

[30]*Pennsylvania State University, University Park, Pennsylvania 16802, USA*

[31]*Institute of High Energy Physics, Protvino 142281, Russia*

[32]*Purdue University, West Lafayette, Indiana 47907, USA*

[33]*Pusan National University, Pusan 609735, Republic of Korea*

[34]*University of Rajasthan, Jaipur 302004, India*

[35]*Rice University, Houston, Texas 77251, USA*

[36]*Universidade de Sao Paulo, CEP 05508-090 Sao Paulo, Brazil*

[37]*University of Science & Technology of China, Hefei 230026, China*

[38]*Shandong University, Jinan, Shandong 250100, China*

[39]*Shanghai Institute of Applied Physics, Shanghai 201800, China*

[40]*SUBATECH, F-44307 Nantes, France*

[41]*Texas A&M University, College Station, Texas 77843, USA*

[42]*University of Texas, Austin, Texas 78712, USA*

[43]*University of Houston, Houston, Texas, 77204, USA*

[44]*Tsinghua University, Beijing 100084, China*

[45]*United States Naval Academy, Annapolis, Maryland 21402, USA*

[46]*Valparaiso University, Valparaiso, Indiana 46383, USA*

[47]*Variable Energy Cyclotron Centre, Kolkata 700064, India*

[48]*Warsaw University of Technology, PL-00-661 Warsaw, Poland*

[49]*University of Washington, Seattle, Washington 98195, USA*

[50]*Wayne State University, Detroit, Michigan 48201, USA*

[51]*Institute of Particle Physics, CCNU (HZNU), Wuhan 430079, China*

[52]*Yale University, New Haven, Connecticut 06520, USA*

[53]*University of Zagreb, Zagreb, HR-10002, Croatia*

[54]*University of Birmingham, Birmingham, B15 2TT United Kingdom*

Two-particle azimuthal ($\Delta\phi$) and pseudorapidity ($\Delta\eta$) correlations using a trigger particle with large transverse momentum (p_T) in d+Au, Cu+Cu, and Au+Au collisions at $\sqrt{s_{NN}} = 62.4$ GeV and 200 GeV from the STAR experiment at the Relativistic Heavy Ion Collider are presented. The near-side correlation is separated into a jet-like component, narrow in both $\Delta\phi$ and $\Delta\eta$, and the ridge, narrow in $\Delta\phi$ but broad in $\Delta\eta$. Both components are studied as a function of collision centrality, and the jet-like correlation is studied as a function of the trigger and associated p_T. The behavior of the jet-like component is remarkably consistent for different collision systems, suggesting it is produced by fragmentation. The width of the jet-like correlation is found to increase with the system size. The ridge, previously observed in Au+Au collisions at $\sqrt{s_{NN}} = 200$ GeV, is also found in Cu+Cu collisions and in collisions at $\sqrt{s_{NN}} = 62.4$ GeV, but is found to be substantially smaller at $\sqrt{s_{NN}} = 62.4$ GeV than at $\sqrt{s_{NN}} = 200$ GeV for the same average number of participants ($\langle N_{\mathrm{part}} \rangle$). Measurements of the ridge are compared to models.

I. INTRODUCTION

Jets are a useful probe of the hot, dense medium created in heavy-ion collisions at the Relativistic Heavy Ion Collider (RHIC) at Brookhaven National Laboratory (BNL). Jet quenching [1] was first observed as the suppression of inclusive hadron spectra at large transverse momenta (p_T) in central Au+Au collisions with respect to p+p data scaled by number of binary nucleon-nucleon collisions [2–7]. Properties of jets at RHIC have been studied extensively using dihadron correlations relative to a trigger particle with large transverse momentum [8–14].

Systematic studies of associated particle distributions on the opposite side of the trigger particle revealed their significant modification in Au+Au relative to p+p and d+Au collisions at the top RHIC energy of $\sqrt{s_{NN}} = 200$ GeV. For low $p_T^{\text{associated}}$, the amplitude of the away-side peak is greater and the shape is modified in Au+Au collisions [8,9]. At intermediate p_T ($4 < p_T^{\text{trigger}} < 6$ GeV/c, 2 GeV/$c < p_T^{\text{associated}} < p_T^{\text{trigger}}$), the away-side correlation peak is strongly suppressed [10]. At higher p_T, the away-side peak reappears without shape modification, but the away-side per trigger yield is smaller in Au+Au collisions than in p+p and d+Au [11].

The associated particle distribution on the near side of the trigger particle, the subject of this paper, is also significantly modified in central Au+Au collisions. In p+p and d+Au collisions, there is a peak narrow in azimuth ($\Delta\phi$) and pseudorapidity ($\Delta\eta$) around the trigger particle, which we refer to as the jet-like correlation. This peak is also present in Au+Au collisons, but an additional structure which is narrow in azimuth but broad in pseudorapidity has been observed in central Au+Au collisions at $\sqrt{s_{NN}} = 200$ GeV [8,12–14]. This structure, called the ridge, is independent of $\Delta\eta$ within the Solenoidal Tracker at RHIC (STAR) acceptance, $|\Delta\eta| < 2.0$, within errors, and persists to high p_T ($p_T^{\text{trigger}} \approx 6$ GeV/c, $p_T^{\text{associated}} \approx 3$ GeV/c). While the spectrum of particles in the jet-like correlation becomes flatter with increasing p_T^{trigger}, the slope of the spectrum of particles in the ridge is independent of p_T^{trigger} and closer to the inclusive spectrum than to that of the jet-like correlation. Recent studies of dihadron correlations at lower transverse momenta ($p_T^{\text{trigger}} > 2.5$ GeV/c, $p_T^{\text{associated}} > 20$ MeV/c) by the PHOBOS experiment show that the ridge is roughly independent of $\Delta\eta$ and extends over four units in $\Delta\eta$ [15]. A similar broad correlation in pseudorapidity is also evident in complementary studies of minijets using untriggered dihadron correlations [16,17].

Several mechanisms for the production of the ridge have been proposed since the first observation of this new phenomenon. In one model [18] the ridge is proposed to be formed from gluon radiation emitted by a high-p_T parton propagating in the medium with strong longitudinal flow. The momentum-kick model proposes that the ridge forms as a fast parton traveling through the medium loses energy through collisions with partons in the medium, causing those partons to be correlated in space with the fast parton [19–21]. Parton recombination has been also proposed as a mechanism for the production of the ridge [22–24]. Another model [25,26] suggests that the ridge is not actually caused by a hard parton but is the product of radial flow and the surface biased emission

of the trigger particle, causing an apparent correlation between particles from the bulk and high-p_T trigger particles.

Another class of models is based on the conversion of correlations in the initial state into momentum space through various flow effects. The model in Ref. [27] explains the ridge as arising from the spontaneous formation of extended color fields in a longitudinally expanding medium due to the presence of plasma instabilities. Long-range pseudorapidity correlations formed in an initial-state glasma combined with radial flow have been also discussed as a mechanism for the ridge [28–30]. Recently, it has been suggested that triangular anisotropy in the initial collision geometry caused by event-by-event fluctuations can give rise to triangular flow, which leads to the ridge and contributes to the double peaked away-side observed in heavy-ion collisions at RHIC [31–37].

In this paper we present measurements of the system size and collision energy dependence of near-side dihadron correlations using data from Cu+Cu and Au+Au collisions at $\sqrt{s_{NN}} = 62.4$ GeV and $\sqrt{s_{NN}} = 200$ GeV measured by the STAR experiment at RHIC. In particular, we investigate the centrality dependence of the jet-like correlations and the ridge and the transverse-momentum dependence of the jet-like correlations. The properties of jet-like correlations in heavy-ion collisions are compared to those from d+Au collisions and PYTHIA simulations to look for possible medium modifications and broadening of the near-side jet-like correlation, for example, due to gluon bremsstrahlung [18]. The new results on the system size and energy dependence of the ridge yield presented in this article extend our knowledge of this phenomenon and, in combination with other measurements at RHIC, provide important quantitative input and constraints to model calculations.

II. EXPERIMENTAL SETUP AND DATA SAMPLE

The results presented in this paper are based on data measured by the STAR experiment from d+Au collisions at $\sqrt{s_{NN}} = 200$ GeV in 2003, Au+Au collisions at $\sqrt{s_{NN}} = 62.4$ GeV and 200 GeV in 2004, and Cu+Cu collisions at $\sqrt{s_{NN}} = 62.4$ GeV and 200 GeV in 2005. The d+Au events were selected using a minimally biased (MB) trigger requiring at least one beam-rapidity neutron in the zero degree calorimeter (ZDC), located at 18 m from the nominal interaction point in the Au beam direction, accepting 95±3% of the Au+Au hadronic cross section [38]. For Cu+Cu collisions, the MB trigger was based on the combined signals from the beam-beam counters (BBC) at forward rapidity ($3.3 < |\eta| < 5.0$) and a coincidence between the ZDCs. The MB trigger for Au+Au collisions at $\sqrt{s_{NN}} = 62.4$ GeV and 200 GeV was obtained using a ZDC coincidence, a signal in both BBCs and a minimum charged particle multiplicity in an array of scintillator slats arranged in a barrel, the central trigger barrel (CTB), to reject nonhadronic interactions. For Au+Au collisions at $\sqrt{s_{NN}} = 200$ GeV, an additional online trigger for central collisions was used. This trigger was based on the energy deposited in the ZDCs in combination with the multiplicity in the CTB. The central trigger sampled the most central 12% of the total hadronic cross section.

TABLE I. Number of events after cuts (see text) in the data samples analyzed.

System	Centrality	$\sqrt{s_{NN}}$ (GeV)	No. of events (10^6)
Cu+Cu	0–60%	62.4	24
Au+Au	0–80%	62.4	8
d+Au	0–95%	200	3
Cu+Cu	0–60%	200	38
Au+Au	0–80%	200	28
Au+Au	0–12%	200	17

In order to achieve a more uniform detector acceptance, only those events with the primary vertex position along the longitudinal beam direction (*z*) within 30 cm of the center of the STAR detector were used for the analysis. For the *d*+Au collisions this was expanded to |*z*| < 50 cm. The number of events after the vertex cut in individual data samples is summarized in Table I.

The STAR time projection chamber (TPC) [39] was used to track charged particles. The collision centrality was determined from the uncorrected number of charged tracks at midrapidity (|η| < 0.5) in the TPC. The charged tracks used for the centrality determination had a three-dimensional distance of closest approach (DCA) to the primary vertex of less than 3 cm and at least 10 fit points from the TPC. Each data sample was then divided into several centrality bins, and the fraction of the geometric cross section, the average number of participating nucleons ($\langle N_{\text{part}} \rangle$), and the average number of binary collisions ($\langle N_{\text{coll}} \rangle$) were calculated using Glauber Monte Carlo model calculations [40].

III. DATA ANALYSIS

A. Correlation technique

Tracks used in this analysis were required to have at least 15 fit points in the TPC, a DCA to the primary vertex of less than 1 cm, and a pseudorapidity |η| < 1.0. As in previous dihadron correlation studies in the STAR experiment [12,41,42], a high-p_T trigger particle was selected and the raw distribution of associated tracks relative to that trigger in pseudorapidity (Δη) and azimuth (Δφ) is studied. This distribution, $d^2 N_{\text{raw}}/d\Delta\phi\, d\Delta\eta$, is normalized by the number of trigger particles, N_{trigger}, and corrected for the efficiency and acceptance of associated tracks ε as follows:

$$\frac{d^2 N}{d\Delta\phi\, d\Delta\eta}(\Delta\phi, \Delta\eta) = \frac{1}{N_{\text{trigger}}} \frac{d^2 N_{\text{raw}}}{d\Delta\phi\, d\Delta\eta}$$
$$\times \frac{1}{\varepsilon_{\text{assoc}}(\phi, \eta)} \frac{1}{\varepsilon_{\text{pair}}(\Delta\phi, \Delta\eta)}. \quad (1)$$

The efficiency correction $\varepsilon_{\text{assoc}}(\phi, \eta)$ is a correction for the TPC single charged track reconstruction efficiency and $\varepsilon_{\text{pair}}(\Delta\phi, \Delta\eta)$ is a correction for track merging and finite TPC track-pair acceptance in Δφ and Δη as described in detail below. The data presented in this paper are averaged between positive and negative Δφ and Δη regions and are reflected about Δφ = 0 and Δη = 0 in the plots.
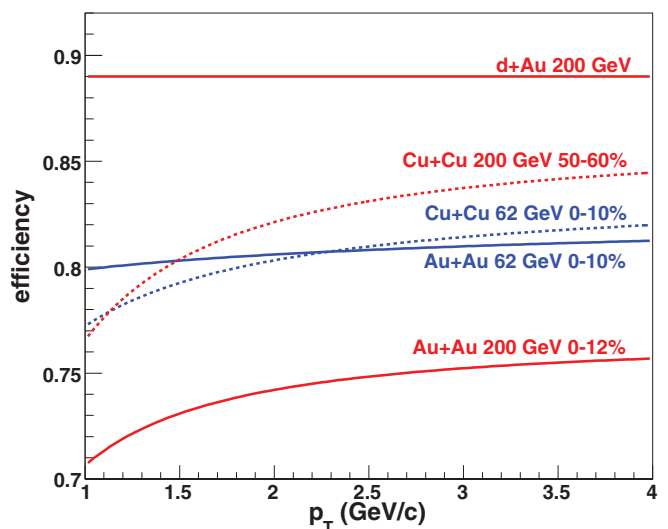

FIG. 1. (Color online) Parameterizations of the transverse-momentum dependence of the reconstruction efficiency of charged particles in the TPC in various collision systems, energies, and centrality bins for the track selection cuts used in this analysis. Note the zero suppression of the axes.

B. Single charged track efficiency correction

The single charged track reconstruction efficiency in the TPC is determined by simulating the detector response to a charged particle and embedding these signals into a real event. This hybrid event is analyzed using the same software as for the real events. The efficiency for detecting a single track as a function of p_T, η, and centrality is determined from the number of simulated particles which were successfully reconstructed. The single track efficiency is approximately constant for $p_T >$ 2 GeV/*c* and ranges from around 75% for central Au+Au events to around 85% for peripheral Cu+Cu events as shown in Fig. 1. The efficiency for reconstructing a track in *d*+Au is 89%. The systematic uncertainty on the efficiency correction, 5%, is strongly correlated across centralities and p_T bins for each data set but not between data sets. In the correlations, each track pair is corrected for the efficiency for reconstructing the associated particle. Since the correlations are normalized by the number of trigger particles, no correction for the efficiency of the trigger particle is necessary.

C. Corrections for track-merging and track-crossing effects in the TPC

The reconstruction of charged tracks from TPC hits is performed iteratively, with hits removed from the event once they are assigned to a track. If two tracks have small angular separation in both pseudorapidity and azimuth, they are more difficult to reconstruct because distinct hits from each particle may not be resolved by the TPC. If two particles are close in momenta or have sufficiently high p_T that their tracks are nearly straight, they may not be distinguished. This effect, called track merging, reduces the number of pairs observed at small opening angles and results in an artificial dip in the raw correlations centered at (Δφ, Δη) = (0,0).
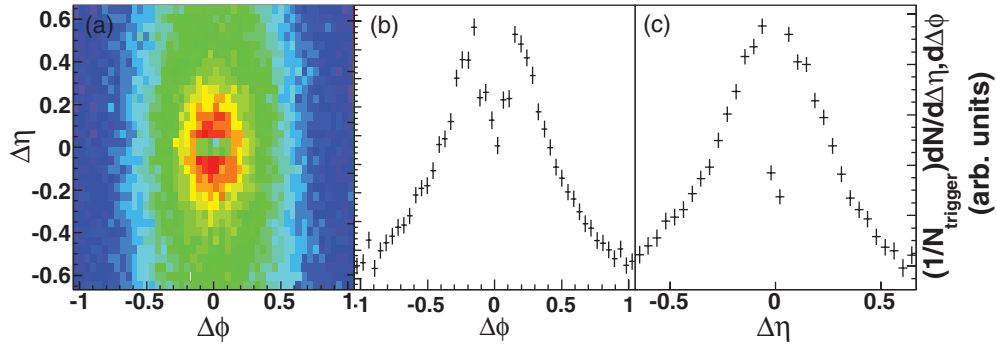
FIG. 2. (Color online) Two-particle dihadron correlation function in $(\Delta\phi, \Delta\eta)$ for $3 < p_T^{\text{trigger}} < 6$ GeV/c and 1.5 GeV/$c < p_T^{\text{associated}} < p_T^{\text{trigger}}$ in 0–12% central Au+Au collisions at $\sqrt{s_{NN}} = 200$ GeV, not corrected for track merging (a). The projection of the correlation function in $\Delta\phi$ for $|\Delta\eta| < 0.042$ is shown in (b) and the projection in $\Delta\eta$ for $|\Delta\phi| < 0.17$ in (c).

Figure 2 shows an example of a $(\Delta\phi, \Delta\eta)$ two-particle dihadron correlation function in central Au+Au collisions at $\sqrt{s_{NN}} = 200$ GeV, along with the corresponding $\Delta\phi$ and $\Delta\eta$ projections for $3 < p_T^{\text{trigger}} < 6$ GeV/c and 1.5 GeV/$c < p_T^{\text{associated}} < p_T^{\text{trigger}}$. For small angular separations, a clear dip in the raw correlations is visible and must be corrected for in order to extract the yield of associated particles on the near side.

Another similar effect is evident in the active TPC volume from high-p_T tracks which cross. While few hits are lost in this case, one track may lose hits near the crossing point and therefore be split into two shorter tracks. Shorter tracks are less likely to meet the track selection criteria. Track merging and track crossing cause four dips near $(\Delta\phi, \Delta\eta) = (0,0)$ but slightly displaced in $\Delta\phi$. The location and width of these dips in $\Delta\phi$ is dependent on the relative helicities, h, and the p_T intervals of the trigger and associated particles. The helicity h is given by

$$h = \frac{-qB}{|qB|}, \qquad (2)$$

where q is the charge of the particle and B is the magnetic field. The dips for tracks of the same helicity are dominantly due to track merging and the dips for tracks of opposite helicities are dominantly due to track crossing. Figure 3 displays the correlation function from Fig. 2 in four different helicity combinations of trigger and associated particles showing the finer substructure of the dip on the near side. When the helicities of the trigger and associated particles are the same, the percentage of overlapping hits is greater. Because higher-p_T tracks have a smaller curvature, it is more likely for two high-p_T tracks close in azimuth and pseudorapidity to be merged than lower-p_T particles. However, track pairs are lost whether the pair is part of the combinatorial background or part of the signal. This effect means that the magnitude of the dip is greater in central collisions where the background is greater and decreases with increasing p_T because of the decreasing background.

One way to correct for the track-merging effect is to remove pairs from mixed events that would have merged in real data. The environment in mixed events must be similar to real data in order for pair rejection to be accurately reproduced. The

reference multiplicities of both events were required to be within 10 of each other to assure similar track density. In addition, mixed events were required to have vertices within 2 cm of each other along the beam axis in order to ensure similar geometric acceptance to avoid a different dip shape in $\Delta\eta$. In order to calculate accurately the percentage of merged hits, the origin of the associated track was shifted to the vertex of the event which the trigger particle originated from.

Previous analyses of low-momentum tracks have shown that eliminating pairs from both data and mixed events with a fraction of merged hits greater than 10% was sufficient to correct for merging [43]. By discarding pairs with more than
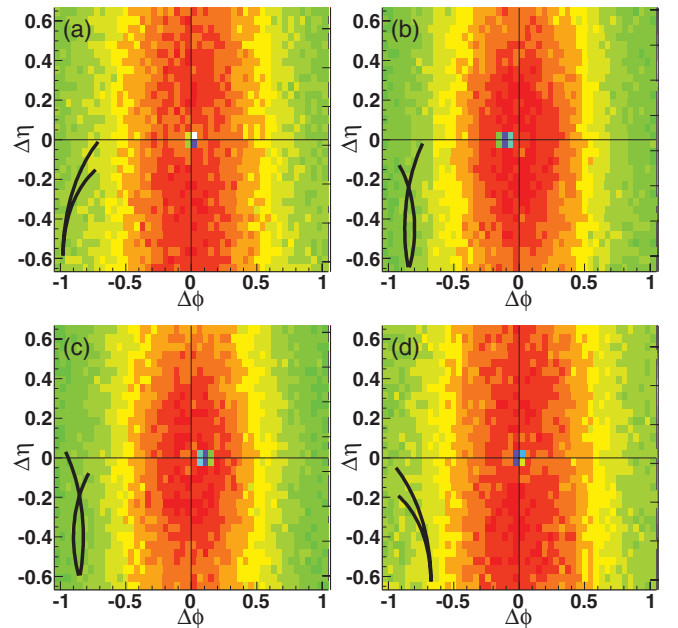
FIG. 3. (Color online) The dip region in $(\Delta\phi, \Delta\eta)$ uncorrected dihadron correlations in 0–12% central Au+Au collisions at $\sqrt{s_{NN}} = 200$ GeV for $3 < p_T^{\text{trigger}} < 6$ GeV/c and 1.5 GeV/$c < p_T^{\text{associated}} < p_T^{\text{trigger}}$ in the four helicity combinations of trigger and associated particles: (a) $(h_{\text{trig}}, h_{\text{assoc}}) = (1, 1)$, (b) $(h_{\text{trig}}, h_{\text{assoc}}) = (1, -1)$, (c) $(h_{\text{trig}}, h_{\text{assoc}}) = (-1, 1)$, and (d) $(h_{\text{trig}}, h_{\text{assoc}}) = (-1, -1)$. Cartoons indicate which dips are from track merging and which are from track crossing.
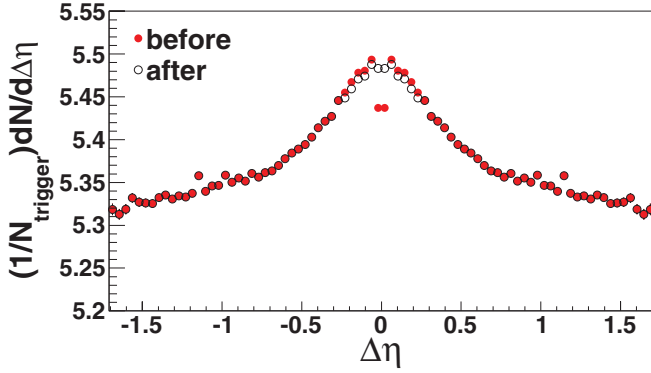
FIG. 4. (Color online) The raw correlation in $\Delta\eta$ for dihadron correlations for $3 < p_T^{\text{trigger}} < 6$ GeV/c and 1.5 GeV/$c < p_T^{\text{associated}} < p_T^{\text{trigger}}$ for 0–12% central Au+Au collisions for $|\Delta\phi| < 0.78$ before and after the track-merging correction is applied. The data have been reflected about $\Delta\eta = 0$.

10% shared hits we ensure that the percentage of merged track pairs is the same in the data and the mixed events.

The correlation function for a given helicity combination of trigger and associated particles was corrected by mixed events. After this correction, a small residual dip remains, mostly due to track crossing. While the mixed events correct for the dip due to true track merging well, they do not correct for track crossing as well. The remaining dip is then corrected for using the symmetry of the correlations. Since the data should be symmetric about $\Delta\phi = 0$, the data on the same side as the dip are discarded and replaced by the data on the side without the dip. Then the data are reflected about $\Delta\eta = 0$ and added to the unreflected data to minimize statistical fluctuations. This method is applied only to $|\Delta\phi| < 1.05$ and $|\Delta\eta| < 0.67$, the region shown in Fig. 2, because it is computationally intensive and track merging and track crossing affect only small angular separations. For large $\Delta\phi$ and $\Delta\eta$, the method described in the next section is applied. The track-merging correction is done for each dihadron correlation function separately with the appropriate cuts on p_T^{trigger}, $p_T^{\text{associated}}$, and collision centrality. An example of the dihadron correlation function before and after the track-merging correction is shown in Fig. 4. The slight decrease in the correlation function for some data points is an artifact of the correction procedure and reflects the uncertainty in the correction.

D. Pair acceptance correction

With the restriction that each track falls within $|\eta| < 1.0$, there is a limited acceptance for track pairs. For $\Delta\eta \approx 0$, the geometric acceptance of the TPC for track pairs is $\approx 100\%$; however, near $\Delta\eta \approx 2$ the acceptance is close to 0%. In azimuth the acceptance is limited by the 12 TPC sector boundaries, leading to dips in the acceptance of track pairs in azimuth. To correct for the geometric acceptance, the distribution of tracks as a function of η and ϕ was recorded for both trigger and associated particles. A random η and ϕ was chosen from each of these distributions to reconstruct a random $\Delta\eta$ and $\Delta\phi$ for each selection of p_T^{trigger}, $p_T^{\text{associated}}$, and centrality. This was

done for at least 4 times as many track pairs as in the data and was used to calculate the geometrical acceptance correction for pairs.

E. Subtraction of anisotropic elliptic flow background

Correlations of particles with the event plane due to anisotropic flow (v_2) in heavy-ion collisions are indirectly reflected in dihadron correlations and have to be subtracted for studies of the ridge. This background in $\Delta\phi$ over the interval $[-a, a]$ is approximated by

$$
\begin{aligned}
&B_{\Delta\phi}[-a, a] \\
&\equiv b_{\Delta\phi} \int_{-a}^{a} d\Delta\phi \left(1 + 2\langle v_2^{\text{trig}}\rangle\langle v_2^{\text{assoc}}\rangle \cos(2\Delta\phi)\right),
\end{aligned} \tag{3}
$$

where a is chosen to be 0.78 so the majority of the signal is contained [12,41]. The level $b_{\Delta\phi}$ of the background is determined using the zero yield at minimum (ZYAM) method [8]. The level of the background is taken as the value of the minimum bin. The systematic errors due to the choice of the minimum bin rather than either of the two neighboring bins are negligible compared to the systematic errors due to the magnitude of v_2, discussed below.

The ZYAM method is commonly used for dihadron correlations at RHIC, for example [8,11,44], and is justified if the near- and away-side peaks are separated by a "signal-free" region. At lower transverse momenta ($p_T < 2$ GeV/c) and in central Au+Au collisions at $\sqrt{s_{NN}} = 200$ GeV, the broadening of the away-side correlation peak may cause overlap of the near- and away-side peaks and, consequently, makes the ZYAM normalization procedure biased. Alternatively, a decomposition of the correlation function using a fit function containing the anisotropic flow modulation of the combinatorial background and components describing the shape of the correlation peaks could be used as well [45,46]. In this paper we use the ZYAM prescription to remain consistent with our earlier measurements of the near-side ridge [12]. ZYAM used with conservative bounds on v_2 will, if anything, underestimate the ridge yield.

For all collision systems and energies studied, the uncertainty bounds on v_2 were determined by comparing different methods for the v_2 measurement. We assume that the error on the v_2 of the trigger and associated particles is 100% correlated. Event-plane measurements of flow and two-particle measurements such as the two-particle cumulant method are sensitive to nonflow from sources such as jets. These methods may overestimate v_2. Methods such as the four-particle cumulant method are less sensitive to contributions from jets; however, these methods may oversubtract contributions from event-by-event fluctuations in v_2. Therefore, these methods underestimate the v_2 that should be used for the background subtraction in dihadron correlations [47]. For each system at least one measurement which may overestimate v_2 and at least one measurement which may underestimate v_2 is included. v_2 and systematic errors on v_2 for Au+Au collisions at $\sqrt{s_{NN}} = 62.4$ GeV are from comparisons of the event-plane method using the forward TPCs for the event-plane determination and the four-particle cumulant method [48]. The v_2 and systematic

errors on v_2 for Au+Au collisions at $\sqrt{s_{NN}} = 200$ GeV are as described in Ref. [12]. The upper bound on v_2 is from the event-plane method using the forward TPCs for the determination of the event plane, the lower bound comes from the four-particle cumulant method, and the average of the two is the nominal value. v_2 for Cu+Cu collisions at $\sqrt{s_{NN}} = 62.4$ GeV and 200 GeV is from Ref. [49]. The nominal value is given by v_2 from the event-plane method using the forward TPCs for the determination of the event plane and the upper bound is from the statistical error for both $\sqrt{s_{NN}} = 62.4$ GeV and 200 GeV. For Cu+Cu collisions measurements using the four-particle cumulant method were not possible due to limited statistics. Instead, for Cu+Cu collisions at $\sqrt{s_{NN}} = 200$ GeV the lower bound is determined by the magnitude of the $\cos(2\Delta\phi)$ term extracted from fits to $p+p$ data, scaling it by $\langle N_{\mathrm{coll}}\rangle$, and subtracting it from v_2 determined using the event-plane method to estimate the maximum contribution from nonflow in Cu+Cu collisions. For Cu+Cu collisions at $\sqrt{s_{NN}} = 62.4$ GeV the systematic error is assumed to be the same in Cu+Cu collisions at both energies.

With both methods for subtracting the ridge contribution to the jet-like yield described below, the systematic errors due to v_2 cancel out in the jet-like yield, assuming that v_2 is independent of $\Delta\eta$ in the TPC acceptance. This assumption is based on the measurements of v_2 as a function of η [50,51].

F. Yield extraction

To quantify the strength of the near-side correlation it is assumed that it can be decomposed into a jet-like component, narrow in both azimuth and pseudorapidity, and a ridge component which is independent of $\Delta\eta$. This approach is consistent with the method in Ref. [12]. For the kinematic cuts applied to p_T^{trigger} and $p_T^{\mathrm{associated}}$, the jet-like correlation is contained within the cuts used in this analysis, $|\Delta\eta| < 0.78$ and $|\Delta\phi| < 0.78$.

To study the jet-like correlation and the ridge quantitatively we adopt the notation from Ref. [12] and introduce the projection of the dihadron correlation function from Eq. (1) onto the $\Delta\eta$ axis as follows:

$$\left.\frac{dN}{d\Delta\eta}\right|_{a,b} \equiv \int_a^b d\Delta\phi \frac{d^2N}{d\Delta\phi d\Delta\eta} \tag{4}$$

and similarly on the $\Delta\phi$ axis,

$$\left.\frac{dN}{d\Delta\phi}\right|_{a,b} \equiv \int_{|\Delta\eta|\in[a,b]} d\Delta\eta \frac{d^2N}{d\Delta\phi d\Delta\eta}. \tag{5}$$

To determine the jet-like yield of associated charged particles two methods are used. The first method is based on $\Delta\phi$ projections. Under the assumption that the jet-like yield is confined within $|\Delta\eta| < 0.78$, subtracting the $\Delta\phi$ projections,

$$\frac{dN_J}{d\Delta\phi}(\Delta\phi) = \left.\frac{dN}{d\Delta\phi}\right|_{0,0.78} - \frac{0.78}{1.0}\left.\frac{dN}{d\Delta\phi}\right|_{0.78,1.78} \tag{6}$$

removes both the elliptic flow and ridge contributions. Since the second $\Delta\phi$ projection is calculated in a larger $\Delta\eta$ window, it has to be scaled by a factor $0.78/1.0$, the ratio of the $\Delta\eta$ width in the region containing the jet-like correlation, the ridge, and

the background to the width of the region containing only the ridge and the background. This subtracts both the ridge and v_2 simultaneously since within errors both are independent of $\Delta\eta$ [12,15,50,51].

The jet-like yield $Y_J^{\Delta\phi}$ is then obtained by integrating Eq. (6)

$$Y_J^{\Delta\phi} = \int_{-0.78}^{0.78} d\Delta\phi \frac{dN_J}{d\Delta\phi}(\Delta\phi). \tag{7}$$

The second method for jet-like yield determination is based on the $\Delta\eta$ projection at the near-side,

$$\frac{dN_J}{d\Delta\eta}(\Delta\eta) = \left.\frac{dN}{d\Delta\eta}\right|_{-0.78,0.78} - b_{\Delta\eta}, \tag{8}$$

as v_2 is independent of pseudorapidity within the STAR acceptance and, therefore, only leads to a constant offset included in $b_{\Delta\eta}$. The background level $b_{\Delta\eta}$ is determined by fitting a constant background $b_{\Delta\eta}$ plus a Gaussian to $\frac{dN_J}{d\Delta\eta}(\Delta\eta)$. The yield determined from fit is discarded to avoid any assumptions about the shape of the peak and, instead, we integrate Eq. (8) over $\Delta\eta$ using bin counting to determine the jet-like yield $Y_J^{\Delta\eta}$:

$$Y_J^{\Delta\eta} = \int_{-0.78}^{0.78} d\Delta\eta \frac{dN_J}{d\Delta\eta}(\Delta\eta). \tag{9}$$

The ridge yield Y_{ridge} is determined by first evaluating Eq. (5) over the entire $\Delta\eta$ region to get $\frac{dN}{d\Delta\phi}$ and then subtracting the modulated elliptic flow background $B_{\Delta\phi}$ and the jet-like contribution $Y_J^{\Delta\eta}$,

$$Y_{\mathrm{ridge}} = \int_{-0.78}^{0.78} d\Delta\phi \left.\frac{dN}{d\Delta\phi}\right|_{0,1.78} - B_{\Delta\phi}[-0.78, 0.78] - Y_J^{\Delta\eta}. \tag{10}$$

We determined the systematic error on the Y_J due to uncertainty in the acceptance correction by comparing the mixed event method described in Sec. III D to the standard event mixing method and to a sample with a restricted z vertex position. The largest difference was seen in the central Au+Au data at $\sqrt{s_{NN}} = 200$ GeV. To be conservative, this difference is used as the systematic error for all the data sets. The resulting systematic errors are listed in Table II. This error is also present for the ridge, since the ridge is determined by subtracting Y_J. Additionally, the systematic error on Y_J due to the track-merging correction does not exceed 1%, the maximum size of the correction in the kinematic region studied in this paper. This correction does not affect Y_{ridge}.

TABLE II. Systematic uncertainties in the acceptance correction.

p_T^{trigger} (GeV/c)	$p_T^{\mathrm{associated}}$ (GeV/c)	Sys. error yield	Sys. error Gaussian width
2.0–2.5	>1.5	<27%	<10%
2.5–3.0	>1.5	<18%	<6%
3.0–6.0	>1.0	<16%	<6%
3.0–6.0	>1.5	<9%	<6%

G. 2D fits

In addition to the standard ZYAM procedure, we also analyzed the distribution of particles in Eq. (1) using two-dimensional fits of the form as follows:

$$
\frac{d^2N}{d\Delta\phi d\Delta\eta} = A \left[1 + \sum_{n=1}^{4} 2V_{n\Delta} \cos(n\Delta\phi) \right]
$$
$$
+ \frac{Y_J}{2\pi \sigma_{\Delta\phi,J}\sigma_{\Delta\eta,J}} e^{-\frac{\Delta\eta}{2\sigma^2_{\Delta\eta,J}}} e^{-\frac{\Delta\phi}{2\sigma^2_{\Delta\phi,J}}}. \quad (11)
$$

with first four coefficients $V_{1\Delta}$, $V_{2\Delta}$, $V_{3\Delta}$, and $V_{4\Delta}$ of a Fourier expansion and a term accounting for the jet-like correlation on the near side. This approach is motivated by the class of models for ridge production through a triangular initial condition. If nonflow contributions are negligible, $V_{2\Delta}$ corresponds to the average of the product of the trigger particle v_2 and the associated particle v_2 and $V_{3\Delta}$ corresponds to the average of the product of the trigger particle v_3 and the associated particle v_3. We use Eq. (11) to fit the data and extract $V_{3\Delta}/V_{2\Delta}$ for all collision energies and systems. We allow $V_{3\Delta}$ to be negative. A narrow roughly Gaussian away-side peak at $\Delta\phi \approx \pi$, which could arise from correlations from the production of an away-side jet, would have a negative contribution to $V_{3\Delta}$ and a negative $V_{3\Delta}$ could indicate that flow is not the dominant production mechanism for these correlations. Furthermore, $V_{2\Delta}$ is not constrained to the experimental values measured for v_2 through other means. There is no systematic error on $V_{3\Delta}/V_{2\Delta}$ due to the efficiency because any uncertainty in the efficiency would change the magnitude of the modulations, given by A in Eq. (11), but not the relative size of those modulations, $V_{2\Delta}$ and $V_{3\Delta}$. The uncertainty due to the fit and uncertainty in the acceptance correction is determined by fixing the parameters within the range given in Table II. This gives an uncertainty of $<4\%$ on $V_{3\Delta}/V_{2\Delta}$.

IV. RESULTS

A. Sample correlations

Figure 5 shows fully corrected $\Delta\eta$ projections of sample correlations on the near side ($|\Delta\phi| < 0.78$) before background subtraction for d+Au, Cu+Cu, and Au+Au collisions at energies $\sqrt{s_{NN}} = 62.4$ GeV and $\sqrt{s_{NN}} = 200$ GeV. The trigger particles were selected with transverse momentum $3 < p_T^{\text{trigger}} < 6$ GeV/c and the associated particles with 1.5 GeV/$c < p_T^{\text{associated}} < p_T^{\text{trigger}}$. The data show a clear jet-like peak sitting on top of the background and the ridge. The level of the background is increasing with energy and system size as expected, as more bulk particles are produced in the collision.

Examples of the complementary projections in $\Delta\phi$ before background subtraction for ($|\Delta\eta| < 1.78$) are shown in Fig. 6. The elliptic flow modulated background is shown as solid curves. The middle curve corresponds to background calculated with the nominal value of v_2. The upper (lower) curve corresponds to the background if the upper (lower) bound on v_2 is used instead. Since we have conservatively assumed that the error on the v_2 of the trigger and associated particles is 100% correlated, the background occasionally goes
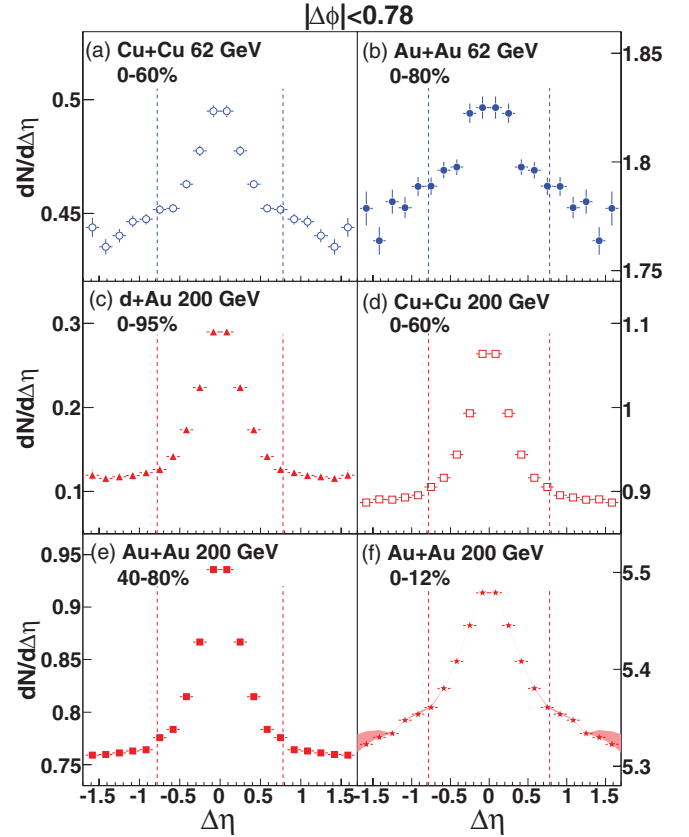

FIG. 5. (Color online) Sample correlations in $\Delta\eta$ ($|\Delta\phi| < 0.78$) for $3 < p_T^{\text{trigger}} < 6$ GeV/c and 1.5 GeV/$c < p_T^{\text{associated}} < p_T^{\text{trigger}}$ for (a) 0–60% Cu+Cu at $\sqrt{s_{NN}} = 62.4$ GeV, (b) 0–80% Au+Au at $\sqrt{s_{NN}} = 62.4$ GeV, (c) 0–95% d+Au at $\sqrt{s_{NN}} = 200$ GeV, (d) 0–60% Cu+Cu at $\sqrt{s_{NN}} = 200$ GeV, (e) 40–80% Au+Au at $\sqrt{s_{NN}} = 200$ GeV, and (f) 0–12% central Au+Au at $\sqrt{s_{NN}} = 200$ GeV. Lines show the $\Delta\eta$ range where the jet-like yield is determined. The data are averaged between positive and negative $\Delta\eta$ and reflected in the plot. Shaded lines in (f) show the systematic errors discussed in Sec. III F.

above the signal in Fig. 6(f) on the away side. However, since we are focusing the near side we prefer this conservative estimate. Note that the uncertainty in the size of the elliptic flow modulated background affects only the ridge yield but not the jet-like yield, since the elliptic flow contribution to the jet-like yield in $\Delta\phi$ cancels out in Eq. (6) and in $\Delta\eta$ is included in $b_{\Delta\eta}$ in Eq. (8).

Sample background-subtracted correlation functions $\frac{dN_J}{d\Delta\eta}$ from Eq. (8) and $\frac{dN_J}{d\Delta\phi}$ from Eq. (6) on the near side for $3 < p_T^{\text{trigger}} < 6$ GeV/c and 1.5 GeV/$c < p_T^{\text{associated}} < p_T^{\text{trigger}}$ from Figs. 5 and 6 are shown in Fig. 7. For the given kinematic selection, the extracted jet-like correlation peaks in both $\Delta\eta$ and $\Delta\phi$ projections look very similar in all studied systems and collision energies. The jet-like yields discussed through the rest of the paper are obtained from the $\Delta\eta$ projection method; the $\Delta\phi$ method is used only for determining the width of the jet-like correlation in $\Delta\phi$. Below, the dependence of the near side jet-like yield and Gaussian width of the jet-like correlation
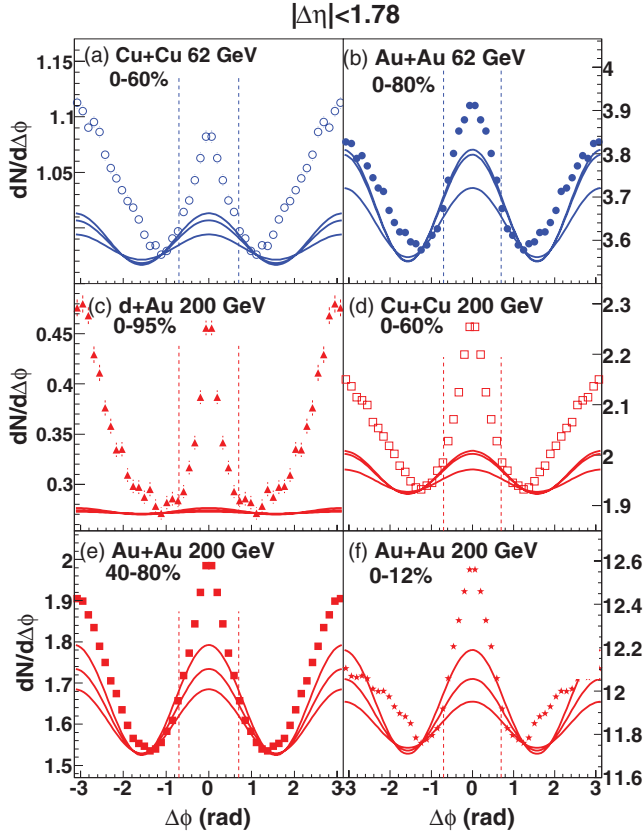
FIG. 6. (Color online) Sample correlations in $\Delta\phi$ ($|\Delta\eta| < 1.78$) for $3 < p_T^{\text{trigger}} < 6$ GeV/c and 1.5 GeV/$c < p_T^{\text{associated}} < p_T^{\text{trigger}}$ for (a) 0–60% Cu+Cu at $\sqrt{s_{NN}} = 62.4$ GeV, (b) 0–80% Au+Au at $\sqrt{s_{NN}} = 62.4$ GeV, (c) 0–95% d+Au at $\sqrt{s_{NN}} = 200$ GeV, (d) 0–60% Cu+Cu at $\sqrt{s_{NN}} = 200$ GeV, (e) 40–80% Au+Au at $\sqrt{s_{NN}} = 200$ GeV, and (f) 0–12% central Au+Au at $\sqrt{s_{NN}} = 200$ GeV. Solid lines show the estimated background using the ZYAM method with the range of v_2 used for the determination of the systematic errors. The data are averaged between positive and negative $\Delta\phi$ and reflected in the plot. Vertical dashed lines show the $\Delta\phi$ range where the jet-like correlation is determined.

peak on collision centrality and the transverse momentum of the trigger and associated particles are studied in detail.

B. The near-side jet-like component

The centrality dependence of the jet-like yield for $3 < p_T^{\text{trigger}} < 6$ GeV/c and 1.5 GeV/$c < p_T^{\text{associated}} < p_T^{\text{trigger}}$ is plotted in Fig. 8. The jet-like yield at $\sqrt{s_{NN}} = 62.4$ GeV is lower than that at $\sqrt{s_{NN}} = 200$ GeV by about a factor of 3, which can be understood as the result of a steeply falling jet spectrum folded with the fragmentation function. The measured yields are compared to PYTHIA simulations shown as a line in Fig. 8. For these studies PYTHIA version 6.4.10 [52] CDF tune A [53], which matches the data from the Tevatron at $\sqrt{s} = 1.8$ TeV and also describes the pion and proton inclusive spectra well at RHIC energies [54–56], is used. The PYTHIA prediction is somewhat above the data, even for d+Au collisions. However, considering the fact that the
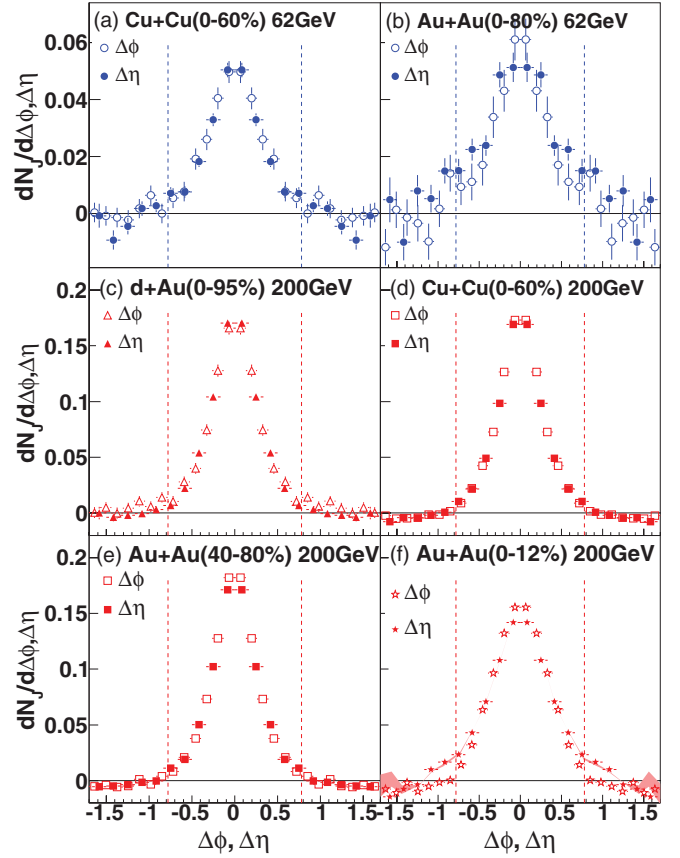
FIG. 7. (Color online) Background-subtracted sample correlations for $3 < p_T^{\text{trigger}} < 6$ GeV/c and 1.5 GeV/$c < p_T^{\text{associated}} < p_T^{\text{trigger}}$ on the near side for (a) 0–60% Cu+Cu at $\sqrt{s_{NN}} = 62.4$ GeV, (b) 0–80% Au+Au at $\sqrt{s_{NN}} = 62.4$ GeV, (c) 0–95% d+Au collisions at $\sqrt{s_{NN}} = 200$ GeV, (d) 0–60% Cu+Cu at $\sqrt{s_{NN}} = 200$ GeV, (e) 40–80% Au+Au at $\sqrt{s_{NN}} = 200$ GeV, and (f) 0–12% central Au+Au at $\sqrt{s_{NN}} = 200$ GeV. The dependence of the jet-like correlation is shown as a function of $\Delta\phi$ ($|\Delta\eta| < 1.78$) in open symbols and of $\Delta\eta$ ($|\Delta\phi| < 0.78$) in closed symbols. Lines show the $\Delta\phi$ and $\Delta\eta$ ranges where the jet-like yield is determined. The data are averaged between positive and negative $\Delta\eta$ ($\Delta\phi$) and reflected in the plot. Lines in (f) show the systematic errors on $\frac{dN_J}{d\Delta\eta}$ discussed in Sec. III F.

data are from heavy-ion collisions and the PYTHIA simulations are for $p + p$ collisions, good agreement is unanticipated. For a given number of participating nucleons, $\langle N_{\text{part}}\rangle$, and collision energy, $\sqrt{s_{NN}}$, there is no significant difference among the d+Au, Cu+Cu, and Au+Au collisions observed, as expected if the jet-like correlation were dominantly produced by vacuum fragmentation.

The dependence of the jet-like yield on p_T^{trigger} for 1.5 GeV/$c < p_T^{\text{associated}} < p_T^{\text{trigger}}$ is plotted in Fig. 9 for all studied collision systems and energies. Data from Au+Au collisions at $\sqrt{s_{NN}} = 200$ GeV are shown separately for peripheral (40–80%) and central (0–12%) Au+Au collisions. The jet-like yield increases constantly with p_T^{trigger} for both Cu+Cu and Au+Au and for $\sqrt{s_{NN}} = 62.4$ GeV and $\sqrt{s_{NN}} = 200$ GeV. The effect of a steeper jet spectrum at $\sqrt{s_{NN}} = 62.4$ GeV relative to 200 GeV discussed above is now reflected in the
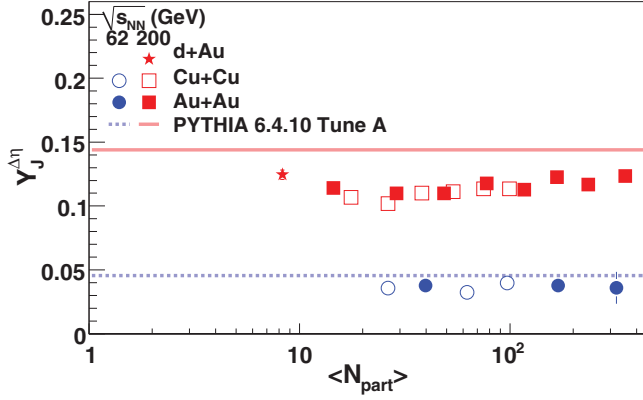
FIG. 8. (Color online) Dependence of jet-like yield on $\langle N_{\text{part}} \rangle$ for $3 < p_T^{\text{trigger}} < 6$ GeV/c and 1.5 GeV/$c < p_T^{\text{associated}} < p_T^{\text{trigger}}$ for Cu+Cu and Au+Au at $\sqrt{s_{NN}} = 62.4$ GeV and d+Au, Cu+Cu, and Au+Au at $\sqrt{s_{NN}} = 200$ GeV. Comparisons to PYTHIA, $\langle N_{\text{part}} \rangle = 2$, are shown as lines. The 5% systematic error due to the uncertainty on the associated particle's efficiency is not shown and systematic errors due to the acceptance correction are given in Table II. The background level and v_2 values used for the extraction of these yields are given in Table IV.

difference between the jet-like yields at the two energies. This difference in the jet-like yield between the two studied collision energies increases with p_T^{trigger} from about a factor of two at $p_T^{\text{trigger}} = 2.5$ GeV/c to a factor of four at $p_T^{\text{trigger}} = 5.5$ GeV/c. Comparisons to PYTHIA simulations are shown as lines in Fig. 9. It is surprising how well PYTHIA is able to describe the p_T^{trigger} dependence of the jet-like yield in $A+A$ collisions. In general, the agreement is better at larger p_T^{trigger} ($p_T^{\text{trigger}} > 4$ GeV/c), while at lower p_T^{trigger} values PYTHIA predicts a larger jet-like yield than observed in the data. No significant differences between d+Au, Cu+Cu, and Au+Au collisions at $\sqrt{s_{NN}} = 200$ GeV are observed. This finding is consistent with the jet-like correlation arising from fragmentation.
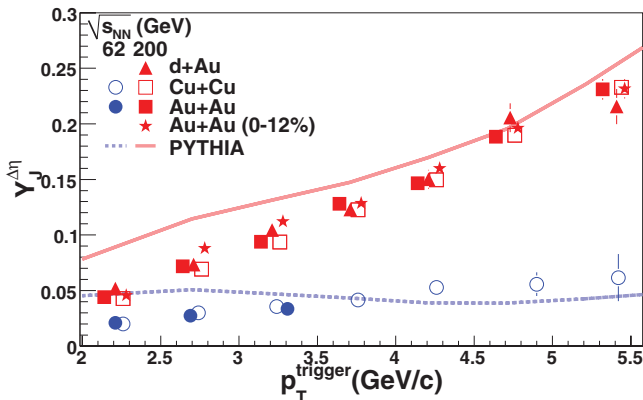

FIG. 9. (Color online) Dependence of jet-like yield on p_T^{trigger} for 0–95% d+Au, 0–60% Cu+Cu at $\sqrt{s_{NN}} = 62.4$ GeV and $\sqrt{s_{NN}} = 200$ GeV, 0–80% Au+Au at $\sqrt{s_{NN}} = 62.4$ GeV, and 0–12% and 40–80% Au+Au at $\sqrt{s_{NN}} = 200$ GeV. Comparisons to PYTHIA are shown as lines. The 5% systematic error due to the uncertainty on the associated particle's efficiency is not shown and systematic errors due to the acceptance correction are given in Table II.

FIG. 10. (Color online) Dependence of jet-like yield on $p_T^{\text{associated}}$ for $3 < p_T^{\text{trigger}} < 6$ GeV/c for (a) 0–60% Cu+Cu and 0–80% Au+Au collisions at $\sqrt{s_{NN}} = 62.4$ GeV and (b) 0–95% d+Au, 0–60% Cu+Cu, 0–12% Au+Au, and 40–80% Au+Au collisions at $\sqrt{s_{NN}} = 200$ GeV. Solid lines through the data points are fits to the data. Comparisons to PYTHIA are shown as dashed lines. The 5% systematic error due to the uncertainty on the associated particle's efficiency is not shown and systematic errors due to the acceptance correction are given in Table II.
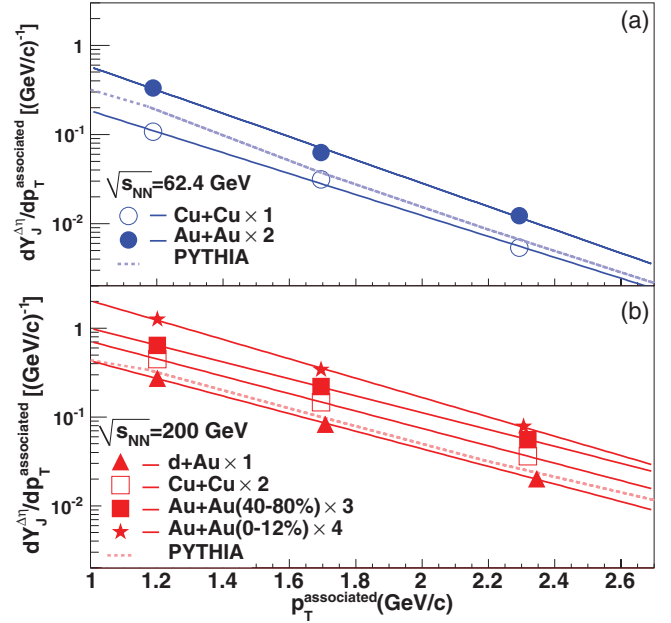
The spectra of particles associated with the jet-like correlation and their comparison to PYTHIA simulations for $3 < p_T^{\text{trigger}} < 6$ GeV/c are shown in Fig. 10. For the same p_T^{trigger} selection, the mean transverse-momentum fraction z_T carried by the leading hadron is larger at $\sqrt{s_{NN}} = 62.4$ GeV than at 200 GeV due to the steeper jet spectrum. This is reflected in softer $p_T^{\text{associated}}$ spectra at $\sqrt{s_{NN}} = 62.4$ GeV. The inverse slope parameters from an exponential fit to these data are shown in Table III. There is no difference seen between Cu+Cu and peripheral Au+Au in either the data points or the extracted inverse slope parameter. The inverse slope parameter of the central Au+Au data at $\sqrt{s_{NN}} = 200$ GeV is somewhat lower than the other data at $\sqrt{s_{NN}} = 200$ GeV, largely because of the larger yield at the lowest $p_T^{\text{associated}}$. This also indicates that there is some modification of the jet-like correlation at low p_T. While the agreement with PYTHIA is remarkable for a comparison to $A+A$ collisions, the discrepancies between PYTHIA and the data are larger at lower momenta and lower energy. This is expected since PYTHIA is tuned better at higher p_T and higher energy.

Figure 11 shows the Gaussian widths of the $\Delta\phi$ and $\Delta\eta$ projections of the near-side jet-like peak as a function of p_T^{trigger}, $p_T^{\text{associated}}$, and $\langle N_{\text{part}} \rangle$ along with PYTHIA simulations. In the most central bin in Au+Au collisions at $\sqrt{s_{NN}} = 62.4$ GeV it was not possible to extract the width in $\Delta\eta$ because of limited statistics combined with a residual track-merging effect. There are no significant differences between the widths as a function of p_T^{trigger} and $p_T^{\text{associated}}$ for different collision systems except

TABLE III. Inverse slope parameters in MeV/c of $p_T^{associated}$ spectra from fits of data in Fig. 10. The inverse slope parameter from a fit to π^- inclusive spectra in Au+Au collisions [57,58] above 1.0 GeV/c is 280.9±0.4 MeV/c for 0–10% $\sqrt{s_{NN}}$ = 62.4 GeV and 330.9±0.3 MeV/c for 0–12% $\sqrt{s_{NN}}$ = 200 GeV. Statistical errors only.

	$\sqrt{s_{NN}}$ = 62.4 GeV	$\sqrt{s_{NN}}$ = 200 GeV
Au+Au	332 ± 13	457 ± 4 (40–80%)
		399 ± 4 (0–12%)
Cu+Cu	370 ± 9	443 ± 3
d+Au		438 ± 9
PYTHIA	417 ± 9	491 ±3

for central Au+Au collisions at $\sqrt{s_{NN}}$ = 200 GeV. While no dependence on collision system is observed, there is a clear increase in the $\Delta\eta$ width with increasing $\langle N_{part}\rangle$ in Au+Au collisions at $\sqrt{s_{NN}}$ = 200 GeV. This indicates that the shape of the jet-like correlation is modified in central Au+Au collisions at $\sqrt{s_{NN}}$ = 200 GeV. PYTHIA predicts a greater width in $\Delta\eta$ at the lowest $p_T^{associated}$ than seen in d+Au or Cu+Cu.

Overall, it can be concluded that the agreement among the different collision systems and energies shows remarkably little dependence of the jet-like per-trigger yield on the system size. In contrast to the peripheral Au+Au data, the central Au+Au data show indications that the jet-like correlation is modified. The model in Ref. [59], a hypothesis for the formation of the ridge through gluon bremsstrahlung, does not produce a ridge broad enough to agree with the data; however, it is possible that a similar mechanism could explain

the broadening of the jet-like correlation. Similarly, models for ridge production by turbulent color fields [27,60] predict a broadening of the jet-like peak in $\Delta\eta$ which is not wide enough to describe the ridge but may explain the data in Fig. 11.

C. The near-side ridge

In Ref. [12], we reported detailed studies of the ridge in Au+Au collisions at $\sqrt{s_{NN}}$ = 200 GeV as a function of $p_T^{trigger}$ and $p_T^{associated}$. Here we investigate the ridge centrality, energy, and system size dependence. The dependence of the ridge yield on $\langle N_{part}\rangle$ for Cu+Cu and Au+Au collisions is shown in Fig. 12 for both energies studied. Table IV shows $b_{\Delta\phi}$ values and v_2 of trigger and associated particles for all collision systems and energies studied in Fig. 12. The centrality bins are characterized by the fraction of geometric cross section σ/σ_{geo}, average number of participants $\langle N_{part}\rangle$, and number of binary collisions $\langle N_{coll}\rangle$. Contrary to the jet-like yield, which shows little dependence on centrality, the ridge yield increases steeply with $\langle N_{part}\rangle$. Within errors, there is no difference in ridge yield between Cu+Cu and Au+Au collisions at the same $\langle N_{part}\rangle$ at a given energy, demonstrating the system independence of the ridge yield.

The energy dependence of the ridge yield is potentially a sensitive test of ridge models. Comparing the two collision energies studied, the ridge yield is observed to be smaller at $\sqrt{s_{NN}}$ = 62.4 GeV than at $\sqrt{s_{NN}}$ = 200 GeV. Similar behavior was also observed for the jet-like yield. Therefore, a closer investigation of the centrality dependence of the ratio Y_{ridge}/Y_{jet} is reported in Fig. 13. The ratio of the yields is independent of collision energy within errors. For the same

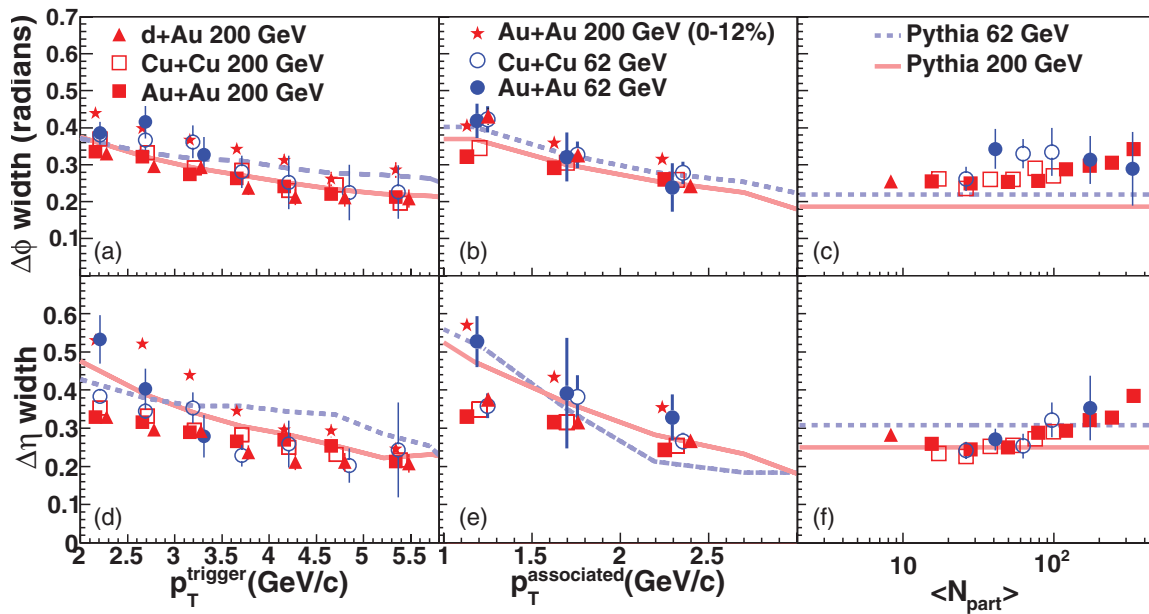FIG. 11. (Color online) Dependence of the widths in $\Delta\phi$ and $\Delta\eta$ on $p_T^{trigger}$ for 1.5 GeV/c < $p_T^{associated}$ < $p_T^{trigger}$, $p_T^{associated}$ for 3 < $p_T^{trigger}$ < 6 GeV/c, and $\langle N_{part}\rangle$ for 3 < $p_T^{trigger}$ < 6 GeV/c and 1.5 GeV/c < $p_T^{associated}$ < $p_T^{trigger}$ for 0–95% d+Au, 0–60% Cu+Cu at $\sqrt{s_{NN}}$ = 62.4 GeV and $\sqrt{s_{NN}}$ = 200 GeV, 0–80% Au+Au at $\sqrt{s_{NN}}$ = 62.4 GeV, and 0–12% and 40–80% Au+Au at $\sqrt{s_{NN}}$ = 200 GeV. Comparisons to PYTHIA are shown as lines. The 5% systematic error due to the uncertainty on the acceptance correction is not shown and systematic errors due to the acceptance correction are given in Table II.

TABLE IV. The background terms $b_{\Delta\phi}$ [see Eq. (3)], elliptic flow values of trigger (v_2^{trigger}) and associated particles (v_2^{assoc}), and Fourier coefficients $V_{2\Delta}$ and $V_{3\Delta}$ from 2D fits for different collision energies, systems and centrality bins defined by the fraction of geometric cross section ($\sigma/\sigma_{\text{geo}}$), average number of participants ($\langle N_{\text{part}}\rangle$) and binary collisions ($\langle N_{\text{coll}}\rangle$) for the data in Figure 8.

System	$\sigma/\sigma_{\text{geo}}$ (%)	$\langle N_{\text{part}}\rangle$	$\langle N_{\text{coll}}\rangle$	$b_{\Delta\phi}$	$\langle v_2^{\text{trigger}}\rangle$ (%)	$\langle v_2^{\text{assoc}}\rangle$ (%)	$V_{2\Delta}$ (%²)	$V_{3\Delta}$ (%²)
d+Au 200 GeV	MB	8.3 ± 0.4	7.5 ± 0.4	0.158 ± 0.006	0.0	0.0	69 ± 1	-285 ± 14
Cu+Cu 62.4 GeV	0–10	96 ± 3	162 ± 14	0.885 ± 0.010	$8.5^{+1.4}_{-2.5}$	$7.3^{+1.9}_{-0.7}$	84 ± 5	54 ± 5
	10–30	64 ± 1	87.9 ± -7.9	0.515 ± 0.006	$11.6^{+0.5}_{-3.2}$	$10.4^{+0.3}_{-1.8}$	228 ± 5	5 ± 5
	30–60	25.7 ± 0.6	27.6 ± 1.6	0.201 ± 0.005	$14.5^{+1.0}_{-5.3}$	$11.8^{+0.3}_{-2.7}$	471 ± 10	-77 ± 10
Au+Au 62.4 GeV	0–10	320 ± 5	800 ± 74	3.582 ± 0.019	$8.5^{+0.3}_{-1.9}$	$7.6^{+0.3}_{-1.9}$	63 ± 3	42 ± 2
	10–40	169 ± 9	345 ± 44	1.846 ± 0.010	$17.5^{+0.3}_{-3.2}$	$15.0^{+0.3}_{-1.9}$	258 ± 2	57 ± 2
	40–80	42 ± 8	51 ± 16	0.446 ± 0.009	$21.2^{+0.3}_{-5.9}$	$18.6^{+0.3}_{-3.4}$	456 ± 8	-33 ± 8
Cu+Cu 200 GeV	0–10	99 ± 1	189 ± 15	1.759 ± 0.007	$8.0^{+0.7}_{-3.0}$	$8.8^{+0.1}_{-2.2}$	128 ± 2	65 ± 1
	10–20	75 ± 1	123.6 ± 9.4	1.206 ± 0.006	$10.5^{+0.6}_{-2.5}$	$11.3^{+0.0}_{-1.8}$	212 ± 2	62 ± 2
	20–30	54 ± 1	77.6 ± 5.4	0.815 ± 0.006	$11.2^{+0.7}_{-2.9}$	$12.5^{+0.1}_{-1.9}$	296 ± 3	47 ± 3
	30–40	38 ± 1	47.7 ± 2.8	0.540 ± 0.006	$10.7^{+0.9}_{-2.6}$	$13.0^{+0.1}_{-2.2}$	380 ± 4	9 ± 4
	40–50	26.2 ± 0.5	29.2 ± 1.6	0.337 ± 0.005	$11.2^{+2.2}_{-6.3}$	$12.6^{+0.5}_{-3.7}$	506 ± 6	-37 ± 6
	50–60	17.2 ± 0.4	16.8 ± 0.9	0.209 ± 0.005	$10.3^{+0.6}_{-2.7}$	$12.3^{+0.0}_{-2.6}$	657 ± 10	-162 ± 10
Au+Au 200 GeV	0–12	316 ± 6	900 ± 71	13.255 ± 0.003	$8.5^{+2.1}_{-2.1}$	$7.3^{+1.5}_{-1.5}$	81 ± 1	49.9 ± 0.2
	10–20	229 ± 5	511 ± 34	4.683 ± 0.007	$14.6^{+2.0}_{-2.0}$	$13.0^{+1.2}_{-1.2}$	225 ± 1	67.1 ± 0.6
	20–30	164 ± 5	325 ± 23	3.222 ± 0.006	$17.8^{+2.1}_{-2.1}$	$16.5^{+1.2}_{-1.2}$	344 ± 1	71.2 ± 0.8
	30–40	114 ± 5	199 ± 16	2.094 ± 0.006	$18.9^{+2.3}_{-2.3}$	$18.1^{+1.4}_{-1.4}$	430 ± 1	68 ± 1
	40–50	76 ± 5	115 ± 12	1.267 ± 0.006	$11.5^{+2.3}_{-2.3}$	$19.0^{+2.5}_{-2.5}$	461 ± 2	57 ± 2
	50–60	48 ± 5	61 ± 8	0.738 ± 0.006	$10.1^{+2.3}_{-2.3}$	$17.6^{+2.8}_{-2.8}$	478 ± 3	18 ± 3
	60–70	28 ± 4	30 ± 5	0.386 ± 0.006	$8.5^{+2.2}_{-2.2}$	$15.4^{+2.9}_{-2.9}$	549 ± 6	-25 ± 6
	70–80	15 ± 2	14 ± 3	0.183 ± 0.006	$6.6^{+1.9}_{-1.9}$	$12.8^{+2.8}_{-2.8}$	754 ± 12	-195 ± 12

kinematic selections, the data at $\sqrt{s_{NN}} = 62.4$ GeV correspond to a lower jet energy which may imply the decrease of the ridge yield with the parton energy, as observed for the jet-like yield.
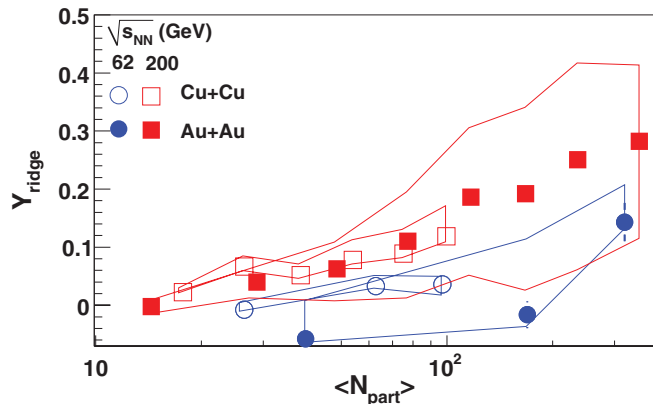
A recent STAR study of the ridge using two-particle azimuthal correlations with respect to the event plane [14] in Au+Au collisions at $\sqrt{s_{NN}} = 200$ GeV shows that the ridge yield is dependent on the angle of the trigger particle relative to the event plane. Another STAR study of three-particle correlations in pseudorapidity [13] in Au+Au collisions at $\sqrt{s_{NN}} = 200$ GeV shows that, within current experimental
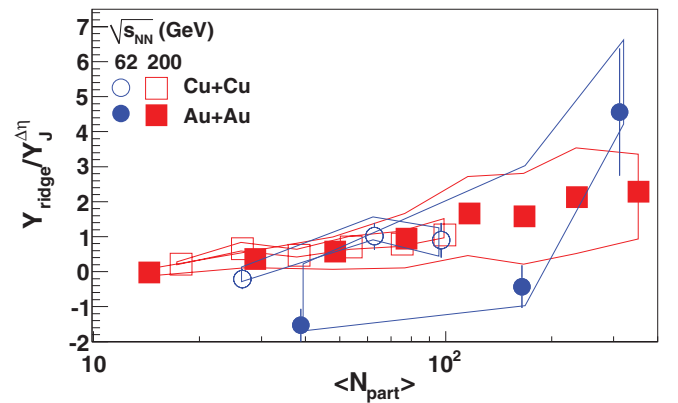

FIG. 12. (Color online) Dependence of the ridge yield on $\langle N_{\text{part}}\rangle$ for $3 < p_T^{\text{trigger}} < 6$ GeV/c and 1.5 GeV/$c < p_T^{\text{associated}} < p_T^{\text{trigger}}$ for Cu+Cu and Au+Au at $\sqrt{s_{NN}} = 62.4$ GeV and Cu+Cu and Au+Au at $\sqrt{s_{NN}} = 200$ GeV. Systematic errors due to v_2 are shown as solid lines. The 5% systematic error due to the uncertainty on the associated particle's efficiency is not shown and systematic errors due to the acceptance correction are given in Table II.

FIG. 13. (Color online) Ratio of the ridge and jet-like yields as a function of $\langle N_{\text{part}}\rangle$ for $3 < p_T^{\text{trigger}} < 6$ GeV/c and 1.5 GeV/$c < p_T^{\text{associated}} < p_T^{\text{trigger}}$. Systematic errors due to v_2 are shown as solid lines and systematic errors due to the acceptance correction are given in Table II.

precision, particles in the ridge are uncorrelated in $\Delta\eta$ with both the trigger particle and each other. These observations along with the PHOBOS measurement of the ridge out to $\Delta\eta = 4$ [15] provide substantial experimental constraints on theories for the production of the ridge. In addition, the CMS experiment recently observed the ridge in high-multiplicity $p+p$ collisions at $\sqrt{s} = 7$ TeV [61]. We consider these results in addition to the results presented in this paper in order to evaluate our current theoretical understanding of the ridge.

The momentum kick model [19] with the same kinematic selection criteria applied to charged particles describes the increase of the ridge yield with centrality quantitatively in Au+Au collisions at $\sqrt{s_{NN}} = 200$ GeV. For a given collision energy the ridge yield for Cu+Cu collisions is predicted to approximately follow that for Au+Au collisions for the same number of participants; however, the prediction for Cu+Cu collisions is systematically above that for Au+Au collisions at both energies. This difference between the two systems is not corroborated by the data. For the same nucleus-nucleus collisions at different energies, the ridge yield in the momentum kick model is predicted to scale approximately with the number of medium partons produced per participant which increases with increasing collision energy as $(\ln\sqrt{s})^2$ [62]. According to this prediction, Y_{ridge} should increase by a factor of 1.6 in collisions at $\sqrt{s_{NN}} = 200$ GeV relative to collisions at 62 GeV. This is in agreement with our measurement. We note that the momentum kick model is likely to have difficulty describing the observed dependence of the ridge yield on the event plane, since it would likely predict a larger ridge out of plane. It would also likely have difficulty explaining the absence of correlations between particles in the ridge and the jet-like correlation.

The model where the ridge arises from the coupling of induced gluon radiation to the longitudinal flow [18] is in qualitative agreement with the observed increase of Y_{ridge} as a function of $\langle N_{\text{part}}\rangle$ since the size of the ridge should depend roughly on the average path length traveled by a hard parton. However, it is not obvious that this model can describe the collision system and energy dependence of ridge yield reported in this paper. Moreover, the large extent of the ridge in $\Delta\eta$ and absence of correlation among ridge particles clearly disfavors this physics mechanism for ridge formation.

The radial flow plus trigger bias model [25,26,63] would predict an increasing ridge yield with increasing N_{part}. This model would predict a larger ridge in plane because of the larger surface area in plane, in agreement with the data. Since the ridge in this model arises from medium partons, particles in the ridge are not expected to be correlated with each other, again, in agreement with the three-particle $\Delta\eta$ correlation data.

The mechanisms for the production of the ridge through glasma initial-state effects [28–30] are able to explain the observed large $\Delta\eta$ extent of the ridge. However, it is not obvious what this class of models would predict for the collision system and energy dependence discussed in this paper as well as for other ridge properties including its p_T^{trigger} and $p_T^{\text{associated}}$ dependence, the event-plane dependence, and the absence of correlated structures in three-particle $\Delta\eta$ correlations. While there are calculations of untriggered

dihadron correlations for the glasma model, there are no calculations to compare to high-p_T triggered correlations. It should be noted that these calculations include not only the glasma initial state but also hydrodynamical flow so some of the ridge in these models is created by flow. If the ridge is produced by the same mechanism in $p+p$ and $A+A$ collisions, models where the ridge is produced by initial-state effects such as the glasma model may be the only models able to explain both the $p+p$ and $A+A$ data simultaneously since hydrodynamical flow in $p+p$ collisions is expected to be small if not negligible. Therefore, quantitative calculations of the ridge in this class of models and the identified particle spectra measurements in high-multiplicity $p+p$ collisions are essential for understanding the production mechanism of the ridge.

Models describing the ridge in terms of quadrupole, triangular, and higher-order components, v_n, from initial eccentricity fluctuations predict a ridge yield that increases with N_{part} [32,34,35,64] in qualitative agreement with the data. Motivated by these models, we applied two-dimensional fits to our data with a two-dimensional Gaussian to describe the jet-like component and $\Delta\eta$ independent $V_{n\Delta}$ terms given by Eq. (11). Figure 14 shows $V_{3\Delta}/V_{2\Delta}$ as a function of $\langle N_{\text{part}}\rangle$ from these fits. The values of the Fourier coefficients $V_{3\Delta}$ and $V_{2\Delta}$ are given in Table IV. We allow $V_{3\Delta}$ to be negative and $V_{3\Delta}$ is negative for $d+$Au collisions and peripheral $A+A$ collisions. An approximately Gaussian peak from an away-side jet-like correlation would give a negative $V_{3\Delta}$ and indicate that $V_{3\Delta}$ is dominantly from nonflow. The ratio $V_{3\Delta}/V_{2\Delta}$ evolves from negative values in $d+$Au and peripheral $A+A$ collisions to positive values at larger $\langle N_{\text{part}}\rangle$.

Positive values for $V_{3\Delta}$ are consistent with expectations from triangular initial conditions. Contributions to a jet-like peak on the away side, such as that observed in $d+$Au, would lead to $V_{3\Delta}/V_{2\Delta} < (v_3/v_2)^2$ because $V_{3\Delta}$ would be an underestimate of v_3^2 and $V_{2\Delta}$ would be an overestimate of v_2^2. For both Au+Au and Cu+Cu collisions, the ratio is independent of collision energy within errors and is largest in the most central collisions with significant deviation between the two colliding systems at the same $\langle N_{\text{part}}\rangle$. It is not clear at this point whether the representation of the data in Fig. 12, where the v_2 has been subtracted, or in Fig. 14, where the v_2 is explicitly included, gives the most insight into the production mechanism of the ridge.

We compare the data to three hydrodynamical models in Fig. 14, noting that these data are in a momentum range approaching the limit where hydrodynamical models are expected to be valid. By comparing different models to the data we are able to see whether the data can constrain the initial state. In Fig. 14(a) we compare the data to 2+1D hydrodynamical model calculations for Au+Au collisions at $\sqrt{s_{NN}} = 200$ GeV for various hadron resonance gas freeze-out temperatures and using a modified Glauber initial state [65]. These calculations use a lattice equation of state and a viscosity to entropy ratio $\eta/s = 1/4\pi$ [66]. We note that this model does not include resonance decays. These predictions agree with the data for all but the three most peripheral centrality bins for a hadron gas freeze-out temperature of 170 MeV.
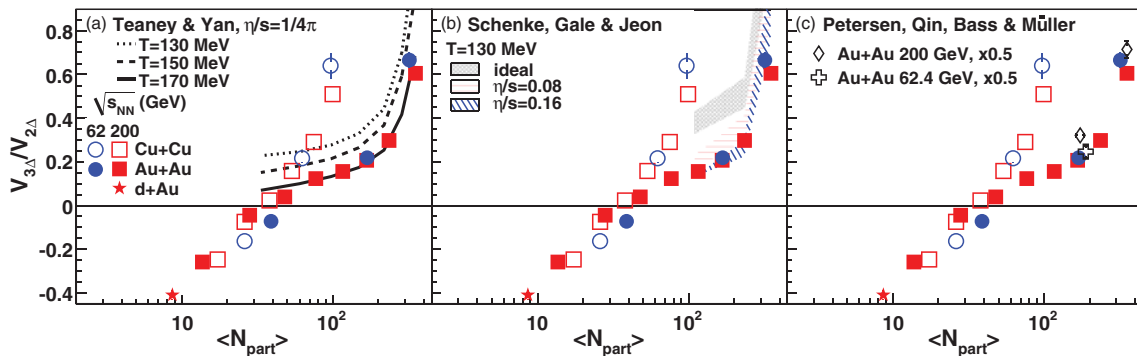
FIG. 14. (Color online) $V_{3\Delta}/V_{2\Delta}$ ratio as a function of $\langle N_{\text{part}} \rangle$ for $3 < p_T^{\text{trigger}} < 6$ GeV/c and 1.5 GeV/$c < p_T^{\text{associated}} < p_T^{\text{trigger}}$. Statistical errors only. The systematic error of $<4\%$ not shown. The data are compared to hydrodynamical calculations using (a) a lattice equation of state with three different freeze-out temperatures in Au+Au collisions at $\sqrt{s_{NN}} = 200$ GeV from Refs. [65,66], (b) using a 3+1D viscous hydrodynamical model with three different viscosity to entropy ratios, η/s [67,68], and (c) a 3+1D model incorporating both hydrodynamics and a transport model [69,70]. In (a) and (c), the same kinematic cuts as the data are used while (b) shows $1.5 < p_T < 4.0$ GeV/c for both p_T^{trigger} and $p_T^{\text{associated}}$.

In Fig. 14(b) we compare the data to 3+1D hydrodynamical model calculations for several values of η/s and a kinetic freeze-out temperature of 130 MeV [67,68]. This model uses a Glauber initial state modified to generate structures like those expected from flux tubes and differs from Ref. [65] because it includes nontrivial longitudinal dynamics and the effect of varying the η/s at a given freeze-out temperature. The calculations in Refs. [67,68] were limited in momentum so it was only possible to compare to calculations with momenta of $1.5 < p_T < 4.0$ GeV/c for both p_T^{trigger} and $p_T^{\text{associated}}$. Qualitatively, this model reproduces the trends observed in the data and it tends to support a higher value of η/s.

Figure 14(c) shows a comparison of the data to a 3+1D event-by-event transport+hydrodynamical model calculation [69,70]. In this model, the initial conditions such as long-range rapidity correlations and fluctuations in the transverse energy density profile are provided by the ultrarelativistic quantum molecular dynamics (UrQMD) model [71,72]. The hydrodynamic evolution starts at 0.5 fm. A transition from hydrodynamic evolution to the transport approach is followed by final-state rescatterings and resonance decays. The predictions shown in the figure are scaled by a factor of 0.5. Requiring a high-p_T trigger particle skews the calculation toward events with a hot spot in the initial density profile, which may lead to a preference for events with a high v_3 value. This model qualitatively describes the $\langle N_{\text{part}} \rangle$ dependence of $V_{3\Delta}/V_{2\Delta}$ for Au+Au collisions at both $\sqrt{s_{NN}} = 62.4$ GeV and 200 GeV.

Despite differences in initial conditions, transport parameters, and freeze-out requirements, all three models shown are able to reproduce the qualitative trends of $V_{3\Delta}/V_{2\Delta}$ versus $\langle N_{\text{part}} \rangle$ for large $\langle N_{\text{part}} \rangle$. Since $V_{3\Delta}$ is expected to be largely independent of centrality [34,73], this likely reflects the model's accuracy in predicting the centrality dependence of $V_{2\Delta}$. The models in Refs. [66,67] reproduce the data fairly well quantitatively, but in Ref. [66] the best fit is achieved by varying the temperature while in Ref. [67] the viscosity varies. Since they also have different initial conditions, we infer that agreement with the data is possible

even with different assumptions and parameters during the hydrodynamical evolution. It will be interesting to see if such similarity persists at lower transverse momenta where the hydrodynamic calculations are more reliable. These studies imply that while fluctuations of the initial state are needed to induce odd higher-order v_n terms, the observable $V_{3\Delta}/V_{2\Delta}$ is rather insensitive to the exact details of the model. This measurement does, however, enforce added restrictions to model implementations and should, therefore, be added to the suite of results, such as identified particle spectra, yields, and p_T dependence of v_2, currently used to validate theories. Future theoretical and experimental studies will be needed to determine whether these models are sufficient to describe the complete ridge and/or whether there are substantial nonflow contributions to the Fourier coefficient $V_{3\Delta}$ in central $A+A$ collisions.

V. CONCLUSIONS

The energy and system size dependence of near-side dihadron correlations enables studies of the jet-like correlation and the ridge at fixed densities with different geometry. The reasonable agreement of the jet-like correlation with PYTHIA is surprising, especially considering that PYTHIA is a $p+p$ event generator. There is remarkably little dependence on the collision system at both $\sqrt{s_{NN}} = 62.4$ GeV and 200 GeV except for central Au+Au collisions at $\sqrt{s_{NN}} = 200$ GeV. In central Au+Au collisions at $\sqrt{s_{NN}} = 200$ GeV the jet-like correlation is substantially broader and the spectrum softer than in peripheral collisions and than those in collisions of other systems in this kinematic regime. This may indicate that fragmentation is modified in these collisions so the parton fragments are softer, perhaps due to a mechanism such as gluon bremsstrahlung. This indicates that the near-side jet-like correlation is dominantly produced by vacuum fragmentation.

The ridge is observed not only in Au+Au collisions at $\sqrt{s_{NN}} = 200$ GeV as we reported earlier but also in Cu+Cu

collisions and in both studied collision systems at lower energy of $\sqrt{s_{NN}} = 62.4$ GeV. This demonstrates that the ridge is not a feature unique to Au+Au collisions at the top RHIC energy. We observe two trends which set significant limits to models. First, when the ridge is measured using the standard ZYAM model, the ridge is comparable in Cu+Cu and Au+Au collisions and the energy dependence of the ridge is the same as the energy dependence of the jet-like correlation. Second, when we subtract the jet-like correlation and calculate the third component of the Fourier decomposition $V_{3\Delta}$, which is v_3^2 in the absence of nonflow, we see different trends for Cu+Cu and Au+Au but no difference between the two energies. The combination of these data with future measurements at lower RHIC energies ($\sqrt{s_{NN}} = 7$–39 GeV) as well as studies at the LHC will, therefore, be a powerful tool for the distinction between various theoretical models for the production of the ridge.

[1] X.-N. Wang and M. Gyulassy, Phys. Rev. Lett. **68**, 1480 (1992).

[2] C. Adler *et al.* (STAR Collaboration), Phys. Rev. Lett. **89**, 202301 (2002).

[3] K. Adcox *et al.* (PHENIX Collaboration), Phys. Rev. Lett. **88**, 022301 (2002).

[4] K. Adcox *et al.* (PHENIX Collaboration), Phys. Lett. B **561**, 82 (2003).

[5] S. S. Adler *et al.* (PHENIX Collaboration), Phys. Rev. Lett. **91**, 072301 (2003).

[6] B. B. Back *et al.* (PHOBOS Collaboration), Phys. Lett. B **578**, 297 (2004).

[7] J. Adams *et al.* (STAR Collaboration), Phys. Rev. Lett. **91**, 172302 (2003).

[8] J. Adams *et al.* (STAR Collaboration), Phys. Rev. Lett. **95**, 152301 (2005).

[9] B. I. Abelev *et al.* (STAR Collaboration), Phys. Rev. Lett. **102**, 052302 (2009).

[10] C. Adler *et al.* (STAR Collaboration), Phys. Rev. Lett. **90**, 082302 (2003).

[11] J. Adams *et al.* (STAR Collaboration), Phys. Rev. Lett. **97**, 162301 (2006).

[12] B. I. Abelev *et al.* (STAR Collaboration), Phys. Rev. C **80**, 064912 (2009).

[13] B. I. Abelev *et al.* (STAR Collaboration), Phys. Rev. Lett. **105**, 022301 (2010).

[14] H. Agakishiev *et al.* (STAR Collaboration) (2010), arXiv:1010.0690 [nucl-ex].

[15] B. Alver *et al.* (PHOBOS Collaboration), Phys. Rev. Lett. **104**, 062301 (2010).

[16] J. Adams *et al.* (STAR Collaboration), Phys. Rev. C **73**, 064907 (2006).

[17] G. Agakishiev *et al.* (STAR Collaboration) (2011), arXive:1109.4380.

[18] N. Armesto, C. A. Salgado, and U. A. Wiedemann, Phys. Rev. Lett. **93**, 242301 (2004).

[19] C.-Y. Wong, Phys. Rev. C **78**, 064905 (2008).

[20] W. Cheuk-Yin, Chin. Phys. Lett. **25**, 3936 (2008).

[21] C.-Y. Wong, Phys. Rev. C **76**, 054908 (2007).

[22] R. C. Hwa and C. B. Yang, Phys. Rev. C **79**, 044908 (2009).

[23] C. B. Chiu, R. C. Hwa, and C. B. Yang, Phys. Rev. C **78**, 044903 (2008).

[24] C. B. Chiu and R. C. Hwa, Phys. Rev. C **79**, 034901 (2009).

[25] S. A. Voloshin, Phys. Lett. B **632**, 490 (2006).

[26] C. A. Pruneau, S. Gavin, and S. A. Voloshin, Nucl. Phys. A **802**, 107 (2008).

[27] A. Majumder, B. Muller, and S. A. Bass, Phys. Rev. Lett. **99**, 042301 (2007).

[28] A. Dumitru, F. Gelis, L. McLerran, and R. Venugopalan, Nucl. Phys. A **810**, 91 (2008).

[29] F. Gelis, T. Lappi, and R. Venugopalan, Phys. Rev. D **79**, 094017 (2009).

[30] S. Gavin, L. McLerran, and G. Moschelli, Phys. Rev. C **79**, 051902(R) (2009).

[31] A. P. Mishra, R. K. Mohapatra, P. S. Saumia, and A. M. Srivastava, Phys. Rev. C **77**, 064902 (2008).

[32] P. Sorensen, J. Phys. G **37**, 094011 (2010).

[33] J. Takahashi *et al.*, Phys. Rev. Lett. **103**, 242301 (2009).

[34] B. Alver and G. Roland, Phys. Rev. C **81**, 054905 (2010).

[35] B. Alver and G. Roland, Phys. Rev. C **82**, 039903(E) (2010).

[36] B. H. Alver, C. Gombeaud, M. Luzum, and J.-Y. Ollitrault, Phys. Rev. C **82**, 034913 (2010).

[37] H. Holopainen, H. Niemi, and K. J. Eskola, Phys. Rev. C **83**, 034901 (2011).

[38] J. Adams *et al.* (STAR Collaboration), Phys. Rev. Lett. **91**, 072304 (2003).

[39] K. H. Ackermann *et al.*, Nucl. Instrum. Methods A **499**, 624 (2003).

[40] M. L. Miller, K. Reygers, S. J. Sanders, and P. Steinberg, Ann. Rev. Nucl. Part. Sci. **57**, 205 (2007).

[41] B. I. Abelev *et al.*, Phys. Lett. B **683**, 123 (2010).

[42] M. M. Aggarwal *et al.* (STAR Collaboration), Phys. Rev. C **82**, 024912 (2010).

[43] J. Adams *et al.* (STAR Collaboration), Phys. Rev. C **71**, 044906 (2005).

[44] A. Adare *et al.* (PHENIX Collaboration), Phys. Rev. C **78**, 014901 (2008).

[45] J. Adams *et al.* (STAR Collaboration), Phys. Rev. C **75**, 034901 (2007).

[46] T. A. Trainor, Phys. Rev. C **81**, 014905 (2010).

[47] S. A. Voloshin, A. M. Poskanzer, and R. Snellings, Springer Materials - The Landolt-Bornstein Database **23** (2010).

[48] B. I. Abelev *et al.* (STAR Collaboration), Phys. Rev. C **75**, 054906 (2007).

[49] B. I. Abelev *et al.* (STAR Collaboration), Phys. Rev. C **81**, 044902 (2010).

[50] B. B. Back *et al.* (PHOBOS Collaboration), Phys. Rev. C **72**, 051901(R) (2005).

[51] B. B. Back *et al.* (PHOBOS Collaboration), Phys. Rev. Lett. **94**, 122303 (2005).

[52] T. Sjöstrand, S. Mrenna, and P. Skands, JHEP 05 (2006) 026.

[53] R. D. Field, eConf C010630 P **501**, (2001).

[54] J. Adams *et al.* (STAR Collaboration), Phys. Rev. D **74**, 032006 (2006).

[55] J. Adams *et al.* (STAR Collaboration), Phys. Lett. B **637**, 161 (2006).

[56] J. Adams *et al.* (STAR Collaboration), Phys. Lett. B **616**, 8 (2005).

[57] B. I. Abelev *et al.* (STAR Collaboration), Phys. Lett. B **655**, 104 (2007).

[58] B. I. Abelev *et al.* (STAR Collaboration), Phys. Rev. Lett. **97**, 152301 (2006).

[59] N. Armesto, C. A. Salgado, and U. A. Wiedemann, Phys. Rev. C **72**, 064910 (2005).

[60] P. Romatschke, Phys. Rev. C **75**, 014901 (2007).

[61] V. Khachatryan *et al.* (CMS Collaboration), JHEP 09 (2010) 091.

[62] W. Busza, Acta Phys. Polon. B **35**, 2873 (2004).

[63] E. V. Shuryak, Phys. Rev. C **76**, 047901 (2007).

[64] P. Sorensen, Nucl. Phys. A **855**, 229 (2011).

[65] D. Teaney and L. Yan, Phys. Rev. C **83**, 064904 (2011).

[66] D. Teaney and L. Yan (private communication).

[67] B. Schenke, S. Jeon, and C. Gale, Phys. Rev. Lett. **106**, 042301 (2011).

[68] B. Schenke (private communication).

[69] H. Petersen, G.-Y. Qin, S. A. Bass, and B. Muller, Phys. Rev. C **82**, 041901(R) (2010).

[70] H. Petersen (private communication).

[71] S. Bass *et al.*, Prog. Part. Nucl. Phys. **41**, 255 (1998).

[72] M. Bleicher *et al.*, J. Phys. G **25**, 1859 (1999).

[73] Z. Qiu and U. W. Heinz, Phys. Rev. C **84**, 024911 (2011).